A physically based distributed karst hydrological model (QMG model-V1.0) for flood simulations

1 **Ji Li[1,*], Daoxian Yuan[1,2], Fuxi Zhang[3], Jiao Liu[4], Mingguo Ma[1]**

2 [1]Chongqing Jinfo Mountain Karst Ecosystem National Observation and Research

3 Station, Chongqing Key Laboratory of Karst Environment, School of Geographical

4 Sciences, Southwest University, Chongqing 400715, China

5 [2]Key Laboratory of Karst Dynamics, MNR & Guangxi, Institute of Karst Geology,

6 Chinese Academy of Geological Sciences, Guilin 541004, China

7 [3]College of Engineering Science and Technology, Shanghai Ocean University;

8 Shanghai Engineering Research Center of Marine Renewable Energy 201306, China

9 [4]Chongqing Municipal Hydrological Monitoring Station, Chongqing 401120, China

10 Corresponding author: Ji Li (445776649@qq.com)

11 **Abstract** Karst trough and valley landforms are prone to flooding, primarily because of the

12 unique hydrogeological features of karst landforms, which are conducive to the spread of rapid

13 runoff. Hydrological models that represent the complicated hydrological processes in karst

14 regions are effective for predicting karst flooding, but their application has been hampered by

15 their complex model structures and associated parameter set, especially for distributed

16 hydrological models, which require large amounts of hydrogeological data. Distributed

17 hydrological models for predicting flooding are highly dependent on distributed modelling,

18 complicated boundary parameter settings, and extensive hydrogeological data processing,

19 which consumes large amounts of both time and computational power. Proposed here is a

20 distributed physically based karst hydrological model, known as the QMG (Qingmuguan)

model. The structural design of this model is relatively simple, and it is generally divided into

surface and underground double-layered structures. The parameters that represent the structural

functions of each layer have clear physical meanings, and fewer parameters are included in this

model than in the current distributed models. This allows karst areas to be modelled with only

a small amount of necessary hydrogeological data. Eighteen flood processes across the karst

underground river in the Qingmuguan karst trough valley are simulated by the QMG model,

and the simulated values agree well with observations: the average value of the Nash–Sutcliffe

coefficient and water balance coefficient is 0.92, while the average relative flow process error

is 10%, and the flood peak error is 11%. A sensitivity analysis shows that the infiltration

coefficient, permeability coefficient, and rock porosity are the parameters that require the most

attention in model calibration and optimization. The improved predictability of karst flooding

by the proposed QMG model promotes a better mechanistic depiction of runoff generation and

confluence in karst trough valleys.

Keywords: Simulation and prediction of karst floods; Karst trough valleys; QMG

(Qingmuguan) model; Parametric optimization; Parameter sensitivity analysis

1 Introduction

Karst trough and valley landforms are very common in China, especially in the southwest. In

general, these karst areas are water scarce during most of the year because their surfaces store

very little rainfall, but they are also potential origins of floods because their trough and valley

landforms and topographic features facilitate the formation and propagation of floods (White,

2002; Li et al., 2021; Gautama et al., 2021). The coexistence of droughts and floods is a typical

phenomenon in these karst trough and valley areas. Taking the example of the present study

area, i.e., the Qingmuguan karst trough valley, floods used to happen constantly during the rainy

season. In recent years, with more extreme rainfall events and the increased area of construction

land in the region, rainfall infiltration has decreased, and rapid runoff over impervious surfaces

has increased, resulting in frequent catastrophic flooding in the basin (Liu et al., 2009). Excess

infiltration runoff from karst sinkholes and underground river outlets often occurs during

flooding (Jourde et al., 2007, 2014; Martinotti et al., 2017), flooding large areas of farmland

and residential areas and causing serious economic losses (Gutierrez, 2010; Parise, 2010; Yu

et al., 2020). Therefore, it is both important and urgent to simulate and predict karst flooding

events in karst troughs and valleys such as those in the study area.

Hydrological models can be effective for forecasting floods and evaluating water resources

in karst areas (Bonacci et al., 2006; Ford and Williams, 2007; Williams, 2008, 2009). However,

modelling floods in karst regions is extremely difficult because of the corresponding complex

hydrogeological structures. Karst water-bearing systems consist of multiple media under the

influence of complex karst development dynamics (Worthington et al., 2000; Kovács and

Perrochet, 2008; Gutierrez, 2010), such as karst caves, conduits, fissures and pores, and are

usually highly spatially heterogeneous (Chang and Liu, 2015; Teixeiraparente et al., 2019;

Zhang et al., 2021). In addition, the intricate surface hydrogeological conditions and the

hydrodynamic conditions inside the karst water-bearing medium result in significant temporal

and spatial differences in the hydrological processes in karst areas (Geyer et al., 2008; Bittner

et al., 2020; Jamal and Awotunde, 2022).

In early studies of flood forecasting in karst regions, simplified lumped hydrological

models were commonly used to describe the rainfall–discharge relationship (e.g., Kovács and

Sauter, 2007; Fleury et al., 2007b; Jukić and Denić, 2009; Hartmann et al., 2014a). With the

development of physical exploration technology and progress in mathematics, computing and

other interdisciplinary disciplines, the level of modelling has gradually improved (Hartmann

and Baker, 2017; Hartmann, 2018; Petrie et al., 2021), and distributed hydrological models have

subsequently become widely applied to karst areas. The main difference between lumped and

distributed hydrological models is that the latter divide the entire basin into many subbasins to

calculate the runoff generation and confluence (Chang et al., 2021; Guila et al., 2022), thereby

better describing the physical properties of the hydrological processes inside a karst water-

bearing system (Jourde et al., 2007; Hartmann, 2018; Epting et al., 2018).

74   Because of their simple structure and low demands for modelling data, lumped

75   hydrological models have been used widely in karst areas (Kurtulus and Razack, 2007;

76   Ladouche et al., 2014). In a lumped model, a river basin is considered as a whole in the

77   calculation of the runoff generation and confluence, and there is no division into subbasins

78   (Dewandel et al., 2003; Bittner et al., 2020). Lumped models usually consider the inputs and

79   outputs of the model (Liedl and Sauter, 2003; Hartmann and Bake, 2013, 2017). In addition,

80   most of the model parameters in a lumped model are not optimized, and the physical meaning

81   of each parameter is unclear (Chen, 2009; Bittner et al., 2020).

82   Distributed hydrological models are of active interest in flood simulation and forecasting

83   research (Ambroise et al., 1996; Beven and Binley, 2006; Zhu and Li, 2014). Compared with

84   that of a lumped model, the structure of a distributed model has a more definite physical

85   significance in terms of its mechanism (Meng and Wang, 2010; Epting et al., 2018). In a

86   distributed hydrological model, an entire karst basin can be divided into many subbasins (Birk

87   et al., 2005) using high-resolution digital elevation model (DEM) data. In the rainfall-runoff

88   algorithm of the model, the hydrogeological conditions and karst aquifer characteristics can be

89   considered fully to precisely simulate the runoff generation and confluence (Martinotti et al.,

90   2017; Gang et al., 2019). The commonly used basin distributed hydrological models (i.e., not

91   special groundwater numerical models, such as MODFLOW) have also been widely applied to

92   karst areas and include the SHE/MIKE and SHE models (Abbott et al., 1986a,b; Doummar

93   et al., 2012), Storm Water Management Model (SWMM) (Peterson and Wicks, 2006; Blansett

94   and Hamlett, 2010; Blansett, 2011), TOPography based hydrological MODEL (TOPMODEL)

95   (Ambroise et al., 1996; Suo et al., 2007; Lu et al., 2013; Pan, 2014) and Soil and Water

96   Assessment Tool (SWAT) (Peterson and Hamlett, 1998; Ren, 2006).

97   The commonly used distributed hydrological models include multiple structures and

98   numerous parameters (Lu et al., 2013; Pan, 2014; Masciopinto et al., 2021), which means that

99   vast amounts of data may be needed to build the model framework in karst regions. For example,

100   the distributed groundwater model MODFLOW-CFPM1 requires detailed data regarding the

101   distribution of karst conduits in the study area (Reimann et al., 2009). Another example is the

102   Karst–Liuxihe model (Li et al., 2019); there are fifteen parameters and five underground

vertical structures in the model. Such a complex structure results in large modelling-data demands, and modelling in karst areas is extremely difficult. In addition, a special borehole pumping test may be required to obtain the rock permeability coefficient.

To overcome the difficulty posed by the large modelling-data demands of distributed hydrological models in karst areas, a new physically based distributed hydrological model—known as the QMG (Qingmuguan) model-V1.0—was developed in the present study. Other commonly used karst groundwater models with complex structures and parameters, such as the aforementioned MODFLOW-CFPM1 model, require considerable hydrogeological data for modelling in karst areas (Qin and Jiang, 2014). The new QMG model has a high potential for application in karst hydrological simulation and prediction. It has certain advantages in terms of its framework and structural design, with a double-layer structure and fewer parameters. The horizontal structure is divided into river channel units and slope units, and the vertical structure below the surface is divided into a shallow karst aquifer and a deep karst aquifer system. This relatively simple model structure reduces the demand for modelling data in karst areas, and only a small amount of hydrogeological data is needed for modelling. To ensure that the QMG model works well in karst flood simulation and prediction despite its relatively simple structure and parameters, we carefully designed the algorithms for runoff generation and confluence in the model. Additionally, to verify the applicability of the QMG model to flood simulation in karst basins, we selected the Qingmuguan karst trough valley in Chongqing, China, as the study area for flood simulation and uncertainty analysis. In particular, we analysed the sensitivity of the model parameters.

2 Study area and data

2.1 Landform and topography

The Qingmuguan karst trough valley is located in the southeastern part of the Sichuan Basin, China, at the junction of the Beibei and Shapingba districts in Chongqing, with coordinates of 29°40′N–29°47′N, 106°17′E–106°20′E. The basin covers an area of 13.4 km^2 and is part of the southern extension of the anticline at Wintang Gorge in the Jinyun Mountains, with the anticlinal axis of Qingmuguan located in a parallel valley in eastern Sichuan (Yang et al., 2008).

131 The surface of the anticline is heavily fragmented, and faults are extremely well developed,

132 with large areas of exposed Triassic carbonate rocks. Under the long-term erosion of karst water,

133 a typical karst trough landform developed (Liu et al., 2009). This karst trough landform

134 provides convenient conditions for flood propagation, and the development of karst landforms

135 is extremely common in the karst region of southwestern China, especially in the karst region

136 of Chongqing.

137 The basin is oriented in a narrow band of slightly curved arcs and is ~12 km long from

138 north to south. The direction of the mountains in the region is generally consistent with the

139 direction of the tectonic line. The catchment area of the basin is mainly composed of the

140 outlying areas of the Lower Triassic Jialingjiang Formation (T1j), the middle Leikoupo

141 Formation (T2l) carbonate rocks on both sides of the mountain slopes, and part of the Upper

142 Xujiahe Formation (T3xj) quartz-sandstone and mudstone (Yang et al., 2008). Tracer tests show

143 that karst development in the underground river system in the study area is strong, where the

144 karst water-bearing medium is heterogeneous and has high water permeability. A large-scale

145 underground river (Fig. 1) with a length of approximately 7.4 km has developed in the karst

146 trough valley, and the flood peak flow of this underground river lasts for a short time.

147 The karst landforms in the area are well developed under closed conditions, and

148 precipitation is the main source of recharge for the underground river system. Most of the

149 precipitation, after evapotranspiration and plant retention are deducted, collects along the slope

150 to the depression at the bottom of the trough and joins the underground river through surface

151 karst fissure dispersion infiltration and concentrated injection in the sinkholes. The map in

152 Figure 1 gives an overview of the Qingmuguan karst basin.

153       **Figure 1.** The Qingmuguan karst basin.

154 **2.2 Hydrogeological conditions**

155 The Qingmuguan basin is located within a subtropical humid monsoon climate zone, with an

156 average temperature of 16.5°C and an average precipitation of 1250 mm concentrated mainly

157 in May–September. An underground river system has developed in the karst trough valley, with

158 a length of 7.4 km, and the water supply of the underground river is mainly rainfall recharge

(Zhang, 2012). Most of the precipitation is collected along the hill slope and routed into the karst depressions at the bottom of the trough valley, where it joins the underground river through the dispersed infiltration of surface karst fissures and sinkholes (Fig. 1a). An upstream surface river collects in a gentle valley and enters the underground river through the Yankou sinkhole (elevation 524 m). Surface water in the middle and lower reaches of the river system enters the underground river system mainly through cover collapse sinkholes (Gutierrez et al., 2014) or fissures.

The stratigraphic and lithologic characteristics of the basin are dominated largely by carbonate rocks of the Lower Triassic Jialingjiang Group (T_{1j}) and Middle Triassic Leikou Slope Group (T_{2l}) on both sides of the slope, with some quartz sandstone and mudstone outcrops of the Upper Triassic Xujiahe Group (T_{3xj}) (Zhang, 2012). The topography of the basin presents a general anticline (Fig. 1b), where carbonate rocks on the surface are corroded and fragmented and have high permeability. Compared with the core of the anticline, the shale of the anticline is less eroded and forms a good waterproof layer.

To investigate the distribution of karst conduits in the underground river system, we conducted a tracer test in the study area. The tracer was placed in the Yankou sinkhole and recovered in the Jiangjia spring (Fig. 1a, c). According to the tracer test results (Gou et al., 2010), the karst water-bearing medium in the aquifer was anisotropic, the karst conduits in the underground river were extremely well developed, and there was a large single-channel underground river approximately five metres wide. The response of the underground river to rainfall was very fast, with the peak flow observed at the outlet of the Jiangjia spring 6–8 h after rainfall based on the tracer test results. The flood peak rose quickly, and the duration of the peak flow was short. The underground river system in the study area is dominated by large karst conduits, which are not conducive to water storage in water-bearing media but are very conducive to the propagation of floods.

2.3 Modelling data

To build the QMG model to simulate karst flood events, the necessary baseline modelling data had to be collected, including 1) high-resolution DEM data and hydrogeological data (e.g.,

187   the thickness of the epikarst zone, rainfall infiltration coefficients of different karst landforms,

188   and rock permeability coefficient); 2) land-use and soil-type data; and 3) rainfall data in the

189   basin and water flow data of the underground river. The DEM data were downloaded from a

190   free database on the public internet, with an initial spatial resolution of 30×30 m. The spatial

191   resolution of the land use and soil types was 1000×1000 m, and they were also downloaded

192   from the internet. After the applicability of modelling and computational strength, as well as

193   the size of the basin in the study area (13.4 km^2), was considered, the spatial resolution of the

194   three types of data was resampled uniformly in the QMG model and downscaled to 15×15 m

195   based on a spatial discrete method by Berry et al. (2010).

196   The hydrogeological data necessary for modelling were obtained in three simple ways. 1)

197   A basin survey was conducted to obtain the thickness of the epikarst zone, which was achieved

198   by observing the rock formations on hillsides following cutting for road construction.

199   Information was collected regarding the location, general shape, and size of karst depressions

200   and sinkholes, which had a significant impact on the compilation of the DEM data and the

201   determination of the convergence process of surface runoff. The sinkholes in the basin are cover

202   collapse sinkholes (Gutierrez et al., 2014) according to the basin survey. There are 3 large

203   sinkholes (more than 3 metres in diameter) and 12 small sinkholes (less than 1 metre in

204   diameter). The remaining 5 sinkholes are between 1 and 3 metres in diameter. The confluence

205   calculation of these sinkholes in the model was based on the results of a previous study (Meng

206   et al., 2009). 2) Empirical equations developed for similar basins were used to obtain the rainfall

207   infiltration coefficients for different karst landforms and the rock permeability coefficient. For

208   example, the rock permeability coefficient was calculated based on an empirical equation from

209   a pumping test in a coal mine in the study area (Li et al., 2019). 3) A tracer experiment was

210   conducted in the study area (Gou et al., 2010) to obtain information on the underground river

211   direction and flow velocity; for instance, underground karst conduits are well developed in the

212   area and form an underground river approximately five metres wide. There are no hydraulic

213   connections between the underground river system in the area and the adjacent basin, which

214   means that there is no overflow recharge.

215   Rainfall and flood data are important model inputs and represent the driving factors that

216 allow hydrological models to operate. In the study area, rainfall data were acquired by two rain

217 gauges located in the basin (Fig. 1a). Point rainfall values were then spatially interpolated into

218 basin-level rainfall (for such a small basin area, rainfall results obtained from two rain gauges

219 were considered representative). There were 18 karst flood events from 14 April 2017 to 10

220 June 2019. We built a rectangular open channel at the underground river outlet and set up a

221 river gauge in it (Fig. 1a) to record the water level and flow data every 15 minutes.

222 **3 Methodology**

223 **3.1 Hydrological model**

224 The hydrological model developed in this study was named the QMG model after the basin for

225 which it was developed and to which it was first applied, i.e., the Qingmuguan basin. The QMG

226 model has a two-layer structure, including a surface part and an underground part. The surface

227 structure is mainly used to perform the calculation of runoff generation and the confluence of

228 the surface river, while the underground structure is used to perform the confluence calculation

229 of the underground river system.

230 The structure of the QMG model is divided into a two-layer structure, both horizontally

231 and vertically. The horizontal structure of the model is divided into river channel units and slope

232 units. The vertical structure below the surface is divided into a shallow karst aquifer (including

233 soil layers, karst fissures and conduit systems in the epikarst zone) and a deep karst aquifer

234 system (bedrock and underground river system). This relatively simple model structure means

235 that only a small amount of hydrogeological data is needed in karst regions. Figure 2 shows a

236 flowchart of the modelling and calculation procedures required for the QMG model.

237 **Figure 2.** Modelling flow chart of the QMG (Qingmuguan) model.

238 To accurately describe the runoff generation and confluence on a grid scale, these karst

239 subbasins are further divided into many karst hydrological response units (KHRUs) based on

240 the high-resolution (15 × 15 m) DEM data in the model. The specific steps involved in the

241 division were adopted by referring to studies of hydrological response units (HRUs) in

242 TOPMODEL by Pan (2014). The KHRUs are the smallest basin computing units; the spatial

243 differences in karst development within the units can be effectively ignored, and the use of these

244 units reduces the uncertainty in the model unit classification. Figure 3 shows the spatial

245 structure of the KHRUs.

246   **Figure 3.** Spatial structure of karst hydrological response units (KHRUs) (Li et al., 2021).

247   The right-hand side of Figure 3 shows a three-dimensional spatial model of KHRUs

248 established in the laboratory to visually reflect the storage and movement of water in the karst

249 water-bearing medium with each spatially anisotropic component and to provide technical

250 support for establishing the hydrological model.

251   The modelling and operation of the QMG model consists of three main stages: 1) spatial

252 interpolation and the retention of rainfall and evaporation calculations; 2) runoff generation and

253 confluence calculation for the surface river; and 3) confluence calculation for the underground

254 runoff, including the confluence in the shallow karst aquifer and the underground river system.

255 **3.1.1 Rainfall and evaporation calculation**

256 In the QMG model, the spatial interpolation of rainfall is accomplished by a kriging method

257 using ArcGIS 10.2 software. The Tyson polygon method may be a simpler method for rainfall

258 interpolation if the number of rainfall gauges in the basin is sufficient. The point rainfall values

259 observed by the two rainfall gauges in the basin (Fig. 1a) were interpolated spatially into an

260 areal rainfall for the entire basin.

261   Basin evapotranspiration in the KHRUs was mainly vegetal evaporation, soil evaporation

262 and water surface evaporation. These components were calculated using the following

263 equations (modified from Li et al., 2020):

264
$$\begin{cases} E_v = V^{t+\Delta t} - V^t - P_v \\ E_s = \lambda E_p, \text{if } F = F_c \\ E_s = \lambda E_p \dfrac{F}{F_c}, \text{if } F < F_{sat} \\ E_w = \Delta e \cdot \left[1.12 + 0.62\left(\Delta T\right)^{0.9}\right] \cdot \left[0.084 + 0.24\left(1 - \gamma^2\right)^{1/2}\right] \cdot \left[0.348 + 0.5\omega^{1.8 - 1.137\omega^{0.05}}\right] \end{cases} \quad (1)$$

265 Here, E_v [mm] is the vegetal discharge, $V^{t+\Delta t} - V^t$ [mm] is the rainfall variation due to

266 vegetation interception, P_v [mm] is the vegetation interception of rainfall and E_s [mm] is

267 the actual soil evaporation. The term λ is the evaporation coefficient. The term E_p [mm] is

268 the evaporation capability, which can be measured experimentally or estimated by the

269 water surface evaporation equation E_w. The term F [mm] is the actual soil moisture, F_{sat}

270 [mm] is the saturation moisture content, F_c [mm] is the field capacity, E_w [mm/d] is the

271 evaporation of the water surface, and $\Delta e = e_0 - e_{150}$ [hPa] is the draught head between the

272 saturation vapour pressure of the water surface and the air vapour pressure 150 m above

273 the water surface. The term $\Delta T = t_0 - T_{150}$ [°C] is the temperature difference between the

274 water surface and the temperature 150 m above the water surface, γ is the relative

275 humidity 150 m above the water surface, and ω [m/s] is the wind speed 150 m above

276 the water surface.

3.1.2 Runoff generation algorithms

278 In the QMG model, the surface runoff generation in river channel units is the rainfall in the

279 river system after evaporation losses are deducted. This portion of the runoff directly

280 participates in the confluence process through the river system rather than undergoing

281 infiltration. In contrast, the process of runoff generation in slope units is more complex, and its

282 classification is related to the developmental characteristics of the surface karst in the basin,

283 rainfall intensity and soil moisture. For example, when the soil moisture content is already

284 saturated, there is the potential for excess infiltration surface runoff in exposed karst slope units.

285 The surface runoff generation of the KHRUs in the river channel units and slope units can be

286 described by the following equations (modified from Chen, 2009, 2018; Li et al., 2020):

287
$$\begin{cases} P_r(t) = \left[P_i(t) - E_p \right] \dfrac{L \cdot W_{max}}{A} \\ R_{si} = (P_i - f_i), P_i \geq f_{max} \\ R_{si} = 0, P_i < f_{max} \\ f_{max} = \alpha (F_c - F)^{\beta} + F_s \end{cases} \tag{2}$$

288 Here, $P_r(t)$ [mm] is the net rainfall (deducting evaporation losses) in the river channel units at

289 time t [h], $P_i(t)$ [mm] is the rainfall in the river channel units, L [m] is the length of the river

290 channel, W_{max} [m] is the maximum width of the river channel selected and A [m²] is the cross-

291 sectional area of the river channel. R_{si} [mm] is termed the excess infiltration runoff in the QMG

292 model when the vadose zone is short of water and has not been filled. The infiltration capacity

293 f_{max} is different for different karst landform units, α and β are the parameters of the Holtan model,

294 and F_s [mm] is the stable depth of soil water infiltration.

295 In the KHRUs (Fig. 3), underground runoff is generated primarily from the infiltration of

296 rainwater and direct confluence recharge from sinkholes or skylights. In the QMG model, the

297 underground runoff is calculated by the following equations (modified from Chen, 2018):

298
$$\begin{cases} R_g = R_0 \exp(-pt^m) \\ R_e = v_e \cdot I_w \cdot z \end{cases} \tag{3}$$

299 where

300
$$\begin{cases} \dfrac{\partial R_e}{\partial x} + I_w \cdot z \cdot \dfrac{\partial F}{\partial t} = R_r - R_{epi} \\ v_e = K \cdot \tan(\alpha), \quad F > F_c \\ v_e = 0, \quad F \le F_c \end{cases} \tag{4}$$

301 Here, R_g [mm] is the underground runoff depth (this part of the underground runoff is mainly

302 from the direct confluence supply of the karst sinkholes or karst windows in the study area), R_0

303 [mm] is the average depth of the underground runoff, p and m are attenuation coefficients

304 calculated by conducting a tracer test in the study area, R_e [L/s] is the underground runoff

305 generated from rainfall infiltration in the epikarst zone, I_w [mm] is the width of the underground

306 runoff on the KHRUs, z [mm] is the thickness of the epikarst zone, R_r [mm^2/s] is the runoff

307 recharge on the KHRUs during period t, R_{epi} [mm^2/s] is the water infiltration from rainfall, v_e

308 [mm/s] is the flow velocity of the underground runoff, K [mm/s] is the current permeability

309 coefficient, and α is the hydraulic gradient of the underground runoff. If the current soil

310 moisture is less than the field capacity, i.e., $F \le F_c$, then the vadose zone is not yet full, no

311 underground runoff is generated, and rainfall infiltration at this time continues to compensate

312 for the lack of water in the vadose zone until it is full and before runoff is generated.

313 **3.1.3 Confluence algorithms**

314 In the QMG model, the calculation of the runoff confluence on the KHRUs includes the

315 confluence of the surface river channel and underground runoff. There are already many mature

316   and classical algorithms available for calculating the runoff confluence in river channel units

317   and slope units, such as the Saint-Venant equations and Muskingum convergence model. In this

318   study, the Saint-Venant equations were adopted to describe the confluence in the surface river

319   and hill slope units, for which a wave movement equation was adopted to calculate confluence

320   in slope units (Chen, 2009):

321
$$\begin{cases} \dfrac{\partial Q}{\partial x} + L\dfrac{\partial h}{\partial t} = q \\ S_f - S_0 = 0 \end{cases} \tag{5}$$

322   where

323
$$Q = vhL = \frac{L}{n}h^{\frac{5}{3}}S_0^{\frac{1}{2}}. \tag{6}$$

324   Here, we customized two variables a and b:

325
$$\begin{cases} a = (\dfrac{n}{L}S_0^{-\frac{1}{2}})^{\frac{3}{5}} \\ b = \dfrac{3}{5} \end{cases} \tag{7}$$

326   Equation (7) was substituted into Eq. (5) and discretized by a finite-difference method,

327   giving

328
$$\begin{cases} \dfrac{\partial Q}{\partial x} + abQ^{(b-1)}\dfrac{\partial Q}{\partial t} - q = 0 \\ \dfrac{\Delta t}{\Delta x}Q_{i+1}^{t+1} + a(Q_{i+1}^{t+1})^b = \dfrac{\Delta t}{\Delta x}Q_i^{t+1} + a(Q_{i+1}^t)^b + q_{i+1}^{t+1}\Delta t \end{cases} \tag{8}$$

329   The Newton–Raphson method was used for iterative calculation using Eq. (8):

330
$$\left[Q_{i+1}^{t+1}\right]^{k+1} = \left[Q_{i+1}^{t+1}\right]^k - \frac{\dfrac{\Delta t}{\Delta x}\left[Q_{i+1}^{t+1}\right]^k + a(\left[Q_{i+1}^{t+1}\right]^k)^b - \dfrac{\Delta t}{\Delta x}Q_i^{t+1} - a(Q_{i+1}^t)^b - q_{i+1}^{t+1}\Delta t}{\dfrac{\Delta t}{\Delta x} + ab(\left[Q_{i+1}^{t+1}\right]^k)^{b-1}}, \tag{9}$$

331   where Q [L/s] is the confluence of water flow in slope units, L [dm] is its runoff width, h [dm]

332   is the runoff depth and q [dm²/s] is the lateral inflow on the KHRUs. Here, the friction slope

333   S_f equals the hill slope S_0, and the inertia term and the pressure term in the motion equation

334   of the Saint-Venant equations were ignored. The term v [dm/s] is the flow velocity of surface

335   runoff in the slope units as calculated by the Manning equation, n is the roughness coefficient

336   of the slope units, Q_i^{t+1} [L/s] is the slope inflow in the KHRU at time $t+1$, and Q_{i+1}^{t+1} [L/s] is

337   the slope discharge in the upper adjacent KHRU at time $t+1$.

338   Similarly, the surface river channel confluence was described based on the Saint-Venant

339   equation, where a diffusion wave movement equation was adopted, meaning that the inertia

340   term in the motion equation was ignored:

341
$$\begin{cases} \dfrac{\partial Q}{\partial x} + \dfrac{\partial A}{\partial t} = q \\[2mm] S_f = S_0 - \dfrac{\partial h}{\partial x} \end{cases} \tag{10}$$

342   A finite-difference method and the Newton–Raphson method were used for the iterative

343   calculation of the above equation:

344
$$\begin{cases} \left[Q_{i+1}^{t+1} \right]^{k+1} = \left[Q_{i+1}^{t+1} \right]^k - \dfrac{\dfrac{\Delta t}{\Delta x}\left[Q_{i+1}^{t+1} \right]^k + c(\left[Q_{i+1}^{t+1} \right]^k)^b - \dfrac{\Delta t}{\Delta x} Q_i^{t+1} - c(Q_{i+1}^t)^b - q_{i+1}^{t+1}\Delta t}{\dfrac{\Delta t}{\Delta x} + cb(\left[Q_{i+1}^{t+1} \right]^k)^{b-1}} \\[4mm] c = (\dfrac{1}{3600} n \chi^{\frac{2}{3}} S_f^{-\frac{1}{2}})^{\frac{3}{5}} \end{cases} \tag{11}$$

345   where Q [L/s] is the water flow in surface river channel units, A [dm^2] is the discharge section

346   area, c is a custom intermediate variable and χ [dm] is the wetted perimeter of the discharge

347   section area.

348   The underground runoff in the model includes the confluence of the epikarst zone and

349   underground river. In the epikarst zone, the karst water-bearing media are highly heterogeneous

350   (Williams, 2008). For example, anisotropic karst fissure systems and conduit systems consist

351   of corrosion fractures. When rainfall infiltrates the epikarst zone, water moves slowly through

352   the small (smaller than 10 cm in this study) karst fissure systems, while it flows rapidly in larger

353   (larger than 10 cm) conduits. The key to determining the confluence velocity lies in the width

354   of karst fractures. In the KHRUs (Fig. 3), a fracture width of 10 cm was used as a threshold

355   value (Atkinson, 1977) based on a borehole pumping test in the basin, meaning that if the

356   fracture width exceeded 10 cm, then the water movement into it was defined as rapid flow;

357   otherwise, it was defined as slow flow. The confluence in the epikarst zone was calculated by

the following equation (modified from Beven and Binley, 2006):

$$Q(t)_{ijk} = b_{ijk} \cdot \frac{\Delta h}{\Delta l} R_i C_j \cdot T(t)_{slow/rapid} \tag{12}$$

where

$$\begin{cases} T(t)_{slow} = nr \dfrac{\rho g R_i C_j L_k}{12v} \\ T(t)_{rapid} = \dfrac{K_{ij}\left(e^{-f_{ij}h_{ij}} - e^{-f_{ij}z_{ij}}\right)}{f_{ij}} \end{cases} \tag{13}$$

Here, $Q(t)_{ijk}$ [L/s] is the flow confluence in the epikarst zone at time t, b_{ijk} [dm] is the

runoff width, $\dfrac{\Delta h}{\Delta l}$ is the dimensionless hydraulic gradient, $T(t)_{slow/rapid}$ is the dimensionless

hydraulic conductivity, ρ [g/L] is the density of the water flow, g [m/s^2] is gravitational

acceleration, n is the valid computational units, $R_i C_j L_k$ [L] is the volume of the ijk-th KHRU,

v is the kinematic viscosity coefficient, f_{ij} is the attenuation coefficient in the epikarst zone, h_{ij}

[dm] is the depth of shallow groundwater, and z_{ij} [dm] is the thickness of the epikarst zone.

The distinction between rapid and slow flows in the epikarst zone is not absolute. The

choice of a 10-cm width karst fracture as the dividing threshold is based on limited evidence

because only five limited boreholes have been tested for pumping in the region. In fact, there is

usually water exchange between the rapid and slow flows at the junction of large and small

fissures in karst aquifers. In the QMG model, this water exchange can be described with the

following equation (modified from Li et al., 2021):

$$\begin{cases} Q = \alpha_{i,j,k}\left(h_n - h_{i,j,k}\right) \\ \alpha_{i,j,k} = \sum_{ip=1}^{np} \dfrac{(K_w)_{i,j,k}\,\pi d_{ip}\,\frac{1}{2}\left(\Delta l_{ip}\tau_{ip}\right)}{r_{ip}} \end{cases} \tag{14}$$

Here, $\alpha_{i,j,k}$ [dm^2/s] is the water exchange coefficient of the ijk-th KHRU, $\left(h_n - h_{i,j,k}\right)$ [dm]

is the water head difference between rapid and slow flows at the junction of large and small

fissures in KHRUs, np is the number of fissure systems connected to the adjacent conduit

378   systems, $(K_w)_{i,j,k}$ [dm/s] is the permeability coefficient at the junction of a fissure and

379   conduit, d_{ip} and r_{ip} [dm] are the conduit diameter and radius, respectively, Δl_{ip} [dm] is

380   the length of the connection between conduits i and p, and τ_{ip} is the conduit curvature. Some

381   of the parameters in this equation, such as $(K_w)_{i,j,k}$ and $(h_n - h_{i,j,k})$, were obtained by

382   conducting an infiltration test in the study area.

383   The confluence of the underground river system plays an important role in the confluence

384   at the basin outlet. To facilitate the calculation of the confluence in the QMG model, the

385   underground river systems can be generalized into large multiple conduit systems. During

386   flooding, these conduit systems are mostly under pressure. Whether the water flow is laminar

387   or turbulent depends on the flow regime at that time. The water flow into these conduits is

388   calculated by the Hagen–Poiseuille equation and the Darcy–Weisbach equation (Shoemaker

389   et al., 2008):

390

$$
\begin{cases}
Q_{\text{laminar}} = -A \dfrac{gd^2 \partial h}{32v \partial x} = -A \dfrac{\rho g d^2 \Delta h}{32 \mu \tau \Delta l} \\[4mm]
Q_{\text{turbulent}} = -2A \sqrt{\dfrac{2gd\left|\Delta h\right|}{\Delta l \tau}} \log \left(\dfrac{H_c}{3.71d} + \dfrac{2.51v}{d\sqrt{\dfrac{2gd^3\left|\Delta h\right|}{\Delta l \tau}}} \right) \dfrac{\Delta h}{\left|\Delta h\right|}
\end{cases}
\tag{15}
$$

391   Here, Q_{laminar} [L/s] is the water flow of the laminar flow in the conduit systems, A [dm^2] is

392   the conduit cross-sectional area, d [dm] is the conduit diameter, ρ [kg/dm^3] is the density of

393   the underground river, $v = \mu / \rho$ is the coefficient of kinematic viscosity, $\Delta h / \tau \Delta l$ is the

394   hydraulic slope of the conduits, τ is the dimensionless conduit curvature, $Q_{\text{turbulent}}$ [L/s] is

395   the turbulent flow in the conduit systems, and H_c [dm] is the average conduit wall height.

396   **3.2 Parameter optimization**

397   In total, the QMG model includes 12 parameters, of which flow direction and slope are

398   topographic parameters that can be determined from the DEM without parametric optimization

399   while the remaining 10 parameters require calibration. Other distributed hydrological models

400   with multiple structures usually have many parameters. For example, the Karst–Liuxihe model

401   (Li et al., 2021) has 15 parameters that must be calibrated. In the QMG model, each parameter

402   is normalized as:

403
$$x_i = x^*_i / x_{i0}, \tag{16}$$

404   where x_i is the dimensionless parameter value i after it is normalized, x^*_i is the parameter

405   value i in actual physical units, and x_{i0} is the initial or final value of x_i. Through the

406   processing of Eq. (16), the value range of the model parameters is limited to a hypercube

407      $K_n = (X \mid 0 \leq x_i \leq 1, i = 1, 2, ..., n)$, and K is a dimensionless value. This normalized treatment

408   ignores the influence of the spatiotemporal variation in the underlying surface attributes on the

409   parameters while also simplifying the classification and number of model parameters to a

410   certain extent. Accordingly, the model parameters can be further divided into rainfall-

411   evaporation parameters, epikarst-zone parameters and underground river parameters. Table 1

412   lists the parameters of the QMG model.

413   **Table 1.** Parameters of the QMG model.

414   Because the QMG model has relatively few parameters, it is possible to calibrate them

415   manually, which means that the operation is easy to implement and does not require a special

416   program for parameter optimization. However, the choice of parameters is subjective, which

417   can lead to great uncertainty in the manual parameter calibration process. To compare the effects

418   of parameter optimization on model performance, this study used both manual parameter

419   calibration and the improved chaotic particle swarm optimization (ICPSO) algorithm for the

420   automatic calibration of model parameters and compared the effects of both on flood simulation.

421   In general, the structure and parameters of a standard particle swarm optimization (PSO)

422   algorithm are simple, with the initial parameter values obtained at random. For parameter

423   optimization in high-dimensional multipeak hydrological models, the standard PSO is easily

424   limited to local convergence and cannot achieve the optimal effect, while the late evolution of

425   the algorithm may also cause problems, such as premature convergence and stagnant evolution,

426   due to the 'inert' aggregation of particles, which seriously affects the efficiency of parameter

427 selection. It is necessary to overcome the above problems and to facilitate a high probability of

428 algorithm convergence to the global optimal solution. In parameter optimization for the QMG

429 model, we improved the standard PSO algorithm by adding chaos theory and developed the

430 ICPSO, where 10 cycles of chaotic disturbances were added to improve the activity of the

431 particles. The inverse mapping equation of the chaotic variable is:

432
$$\begin{cases} X_{ij} = X_{min} + (X_{max} - X_{min}) * Z_{ij} \\ Z'_{ij} = (1-\alpha)Z^* + \alpha Z_{ij} \end{cases} \tag{17}$$

433 where X_{ij} is the optimization variable for the model parameters and $(X_{max} - X_{min})$ is the

434 difference between its maximum and its minimum; Z_{ij} is the variable before the disturbance is

435 added and Z'_{ij} represents the chaotic variables after a disturbance is added; α is a variable

436 determined by the adaptive algorithm, in which $0 \le \alpha \le 1$; and Z^* is the chaotic variable formed

437 when the optimal particle is mapped to the interval [0,1]. The flowchart of the ICPSO for

438 parameter optimization is shown in Figure 4.

439 **Figure 4.** Algorithm flow chart of the improved chaotic particle swarm optimization (ICPSO).

440 **3.3 Uncertainty analysis**

441 Uncertainties in hydrological model simulation results usually originate from three aspects:

442 input data, model structure and model parameters (Krzysztofowicz, 2014). In the present study,

443 the input data (e.g., rainfall, flood events and some hydrogeological data) were first validated

444 and preprocessed through observations to reduce their uncertainties.

445 Second, we simplified the structure of the QMG model to reduce the structural uncertainty.

446 As a mathematical and physical model, a hydrological model has some uncertainty in flood

447 simulation and prediction because of the errors in system structure and the algorithm

448 (Krzysztofowicz and Kelly, 2000). The model was designed with full consideration of the

449 relationship between the amount of data required to build the model and its performance for

450 flood simulation and prediction in karst regions, and the model's entire framework was

451 integrated through simple structures and easy-to-implement algorithms using the concept of

distributed hydrological modelling. Conventionally, the extent of uncertainty increases with the growing complexity of the model structure. We therefore ensured that the structure of the QMG model was simple when it was designed, and the model was divided into surface and underground double-layer structures to reduce its structural uncertainty.

Third, we focused on analysing the uncertainty and sensitivity of the model parameters and their optimization method, for which a multiparametric sensitivity analysis method (Choi et al., 1999; Li et al., 2020) was used to analyse the sensitivity of the parameters in the QMG model. The steps in the parameter sensitivity analysis were as follows.

1) Selection of the appropriate objective function

The Nash–Sutcliffe coefficient is widely used as an objective function to evaluate the performance of hydrological models (Li et al., 2020, 2021). The coefficient was therefore used to assess the QMG model. Because the most important factor in flood prediction is the peak discharge, it is used in the Nash–Sutcliffe coefficient equation:

$$NSC = 1 - \frac{\sum_{i=1}^{n}\left(Q_i - Q_i^{'}\right)^2}{\sum_{i=1}^{n}\left(Q_i - \overline{Q}\right)^2} \tag{18}$$

where NSC is the Nash–Sutcliffe coefficient, Q_i [L/s] represents the observed flow discharges, Q_i' [L/s] represents the simulated discharges, $\overline{Q}$ [L/s] is the average observed discharge and n [h] is the observation period.

2) Parameter sequence sampling

The Monte Carlo sampling method was used to sample 8000 groups of parameter sequences. The parametric sensitivity of the QMG model was analysed and evaluated by comparing the differences between the a priori and a posteriori distributions of the parameters.

3) Parameter sensitivity assessment

The a priori distribution of a model parameter is its probability distribution, while the a posteriori distribution refers to the conditional distribution calculated after sample sampling and can be calculated based on the parametric optimization simulation result. If there is a

477 significant difference between the a priori distribution and the a posteriori distribution of a

478 parameter, then the parameter being tested has a high sensitivity, whereas if there is no obvious

479 difference, then the parameter is insensitive. The parametric a priori distribution is calculated

480 as follows:

481
$$\begin{cases} P_{i,j}(NSC_{i,j} \geq 0.85) = \dfrac{n}{N+1} \times 100 \\ \sigma_i = \sum_{j=1}^{n} \left(P_{i,j} - \overline{P_{i,j}} \right)^2 \end{cases} \tag{19}$$

482 where $P_{i,j}$ is the a priori distribution probability when $NSC_{i,j} \geq 0.85$. We used a simulated

483 Nash–Sutcliffe coefficient of 0.85 as the threshold value, and n was the number of occurrences

484 of a Nash–Sutcliffe coefficient greater than 0.85 in flood simulations. In each simulation, only

485 a certain parameter was changed, while the remaining parameters remained unchanged. If the

486 Nash–Sutcliffe coefficient of this simulation exceeded 0.85, then the flood simulation results

487 were considered acceptable. The term σ_i is the difference between the acceptable value and

488 its mean, which represents the parametric sensitivity ($0 < \sigma_i < 1$). The higher the σ_i value

489 is, the more sensitive the parameter. N is the 8000 parameter sequences, and $\overline{P_{i,j}}$ is the average

490 value of the a priori distribution.

491 **3.4 Model setting**

492 Once the model was built, some of the initial conditions had to be set before running it to

493 simulate and forecast floods, such as basin division, the setting of initial soil moisture, and the

494 assumption of the initial parameter range. 1) In the study area, the entire Qingmuguan karst

495 basin was divided into 893 KHRUs, including 65 surface river units, 466 hill slope units, and

496 362 underground river units. The division of these units formed the basis for calculating the

497 process of runoff generation and convergence. 2) The initial soil moisture was set to 0–100%

498 of the saturation moisture content in the basin, and the specific soil moisture before each flood

499 had to be determined by a trial calculation. 3) The waterhead boundary conditions of the

500 groundwater were determined by a tracer test in the basin, where a perennial stable water level

501 adjacent to the groundwater-divide was used as the fixed waterhead boundary. The base flow

502 of the underground river was determined to be 35 L/s from the perennial average dry season

503 runoff. 4) The range of initial parameters and convergence conditions were assumed before

504 parameter optimization (Fig. 4). 5) Parameter optimization and flood simulation validated the

505 performance of the QMG model in karst basins.

4 Results

4.1 Parameter sensitivity results

508 The number of parameters in a distributed hydrological model is generally large, and it is

509 important to perform a sensitivity analysis on each parameter to quantitatively assess the

510 impacts of the different parameters on model performance. In the QMG model, each parameter

511 was placed into one of four categories according to its sensitivity: (i) highly sensitive, (ii)

512 sensitive, (iii) moderately sensitive, and (v) insensitive. In the calibration of model parameters,

513 insensitive parameters do not need to be calibrated, which can greatly reduce the number of

514 calculations and improve the model operation efficiency.

515 The flow process in the calibration period (14 April to 10 May 2017) was adopted to

516 calculate the sensitivity of the model parameters, where equation (19) was used, and the

517 parameter sensitivity results are presented in Table 2.

Table 2. Parametric sensitivity results of the QMG model.

519 In Table 2, the value of σ_i [equation (19)] represents a parameter's sensitivity, and the

520 higher the value, the more sensitive the parameter is. The results in Table 2 show that the rainfall

521 infiltration coefficient, rock permeability coefficient, rock porosity, and the related parameters

522 of soil water content, such as the saturated water content and field capacity, were sensitive

523 parameters. The order of parameter sensitivities was as follows: infiltration coefficient >

524 permeability coefficient > rock porosity > specific yield > saturated water content > field

525 capacity > flow direction > thickness > slope > soil coefficient > channel roughness >

526 evaporation coefficient.

527 In the QMG model, parameters were classified as highly sensitive, sensitive, moderately

528 sensitive, and insensitive according to their influence on the flood simulation results. In Table 4,

529   we divided the sensitivity of model parameters into four levels based on the σ_i value: 1) highly

530   sensitive parameters, $0.8 < \sigma_i < 1$; 2) sensitive parameters, $0.65 < \sigma_i < 0.8$; 3) moderately

531   sensitive parameters, $0.45 < \sigma_i < 0.65$; and 4) insensitive parameters, $0 < \sigma_i < 0.45$. The

532   infiltration coefficient, permeability coefficient, rock porosity, and specific yield were highly

533   sensitive parameters. The saturated water content, field capacity, and thickness of the epikarst

534   zone were sensitive parameters. The flow direction, slope, and soil coefficient were moderately

535   sensitive parameters. The channel roughness and the evaporation coefficient were insensitive

536   parameters.

537   **4.2 Parametric optimization**

538   In total, the QMG model has 12 parameters, of which only eight need to be optimized, which

539   is relatively few from the perspective of distributed models. The parameters of flow direction

540   and slope as well as the insensitive parameters of channel roughness and the evaporation

541   coefficient do not need to be calibrated, which can improve the convergence efficiency of the

542   model parameter optimization.

543   In the study area, 18 karst floods were recorded at the underground river outlet during the

544   period from 14 April 2017 to 10 June 2019 and used to validate the effects of the QMG model

545   in karst hydrological simulations. The calibration period was from 14 April to 10 May 2017, at

546   the beginning of the flow process, with the remainder of the time being used as the validation

547   period. In the QMG model, the ICPSO algorithm was used to optimize the model parameters.

548   To show the necessity of parameter optimization for the distributed hydrological model, this

549   study specifically compared the flood simulations obtained using the initial parameters of the

550   model (without parameter calibration) and the optimized parameters. Figure 5 shows the

551   iteration process of parameter optimization for the QMG model.

552   **Figure 5**. Iteration process of parametric optimization.

553   Figure 5 shows that almost all parameters fluctuated widely at the beginning of the

554   optimization, and after approximately 15 iterations of optimization calculations, most of the

555   linear fluctuations became significantly less volatile, which indicated that the algorithm was

556 tending towards convergence (possibly only locally). When the number of iterations exceeded

557 25, all parameters remained essentially unchanged, meaning that the algorithm had converged

558 (at this point, there was global convergence). It took only 25 iterations to reach a definite

559 convergence of the parameter rates with the ICPSO algorithm, which is extremely efficient in

560 terms of the parameter optimization of distributed hydrological models. In previous studies of

561 the parametric optimization for the Karst-Liuxihe model in similar basin areas, 50 automatic

562 parameter optimization iterations were required to reach convergence (Li et al., 2021),

563 demonstrating the effectiveness of the ICPSO algorithm.

564 To evaluate the effect of parameter optimization, the convergence efficiency of the

565 algorithm and, more importantly, the parameters after calibration were used to simulate floods.

566 Figure 6 shows the flood simulation effects.

567 **Figure 6**. Flow simulation results of the QMG model based on parameter optimization.

568 Figure 6 shows that the flows simulated by parameter optimization were better than those

569 simulated by the initial model parameters. The simulated flow processes based on the initial

570 parameters were relatively small, with the simulated peak flows in particular being smaller than

571 the observed values, and there were large errors between the two values. In contrast, the

572 simulated flows produced by the QMG model after parameter optimization were very similar

573 to the observed values, which indicated that calibration of the model parameters was necessary

574 and that there was an improvement in parameter optimization through the use of the ICPSO

575 algorithm in this study. In addition, it was found that the flow simulation effect was better in

576 the calibration periods than in the validation periods (Fig. 6).

577 To compare the results of the flow process simulation with the initial model parameters

578 and that with the optimized parameters, six evaluation indices (Nash–Sutcliffe coefficient,

579 correlation coefficient, relative flow process error, flood peak error, water balance coefficient,

580 and peak time error) were applied in this study, and the results are presented in Table 3.

581 **Table 3**. Flood simulation evaluation indices without and with parametric optimization.

582 Table 3 shows that the evaluation indices of the flood simulations after parametric

583 optimization were better than those of the initial model parameters. The average values of the

584 initial parameters for these six indices were 0.81, 0.74, 27%, 31%, 0.80, and 5 h, respectively.

585 For the optimized parameters, the average values were 0.90, 0.91, 16%, 14%, 0.94, and 3 h,

586 respectively. The flood simulation effects after parameter optimization were clearly improved,

587 implying that parameter optimization of the QMG model was necessary and that the ICPSO

588 algorithm was an effective approach for parameter optimization that could greatly improve the

589 convergence efficiency of parameter optimization and ensure that the model performed well in

590 flood simulations.

591 **4.3 Model validation**

592 Following parameter optimization, we simulated the whole flow process (14 April 2017 to 10

593 June 2019) based on the optimized and initial parameters of the QMG model (Fig. 6), which

594 enabled a visual reflection of the application of the model the simulation of a long series of

595 flow processes. To reflect the simulation effects of the model for different flood events, we

596 divided the whole flow process into 18 flood events and then used the initial parameters of the

597 model and the optimized parameters to verify the model performance in flood simulations.

598 Figure 7 and Table 4 show the flood simulation effects and their evaluation indices using both

599 the initial and the optimized parameters.

600 **Figure 7**. Flood simulation effects based on initial and optimized parameters.

601 **Table 4.** Flood simulation indices for model validation.

602 Figure 7 shows that the flood simulation results using the initial parameters were smaller

603 than the observed values and that the model performance in flood simulations improved after

604 parameter optimization. The simulated flood processes were in good agreement with

605 observations and were especially effective for simulating flood peak flows. From the flood

606 simulation indices in Table 4, the average water balance coefficient based on the initial

607 parameters was 0.69, i.e., much less than 1, indicating that the simulated water in the model

608 was unbalanced. After parameter optimization, the average value was 0.92, indicating that

609 parameter optimization had a significant impact on the model water balance calculation.

610 Table 4 shows that the average values of the six indices (Nash–Sutcliffe coefficient,

611 correlation coefficient, relative flow process error, flood peak error, water balance coefficient,

612 and peak time error) for the initial parameters were 0.79, 0.74, 26%, 25%, 0.69, and 5 h,

613 respectively, while for the optimized parameters, the average values were 0.92, 0.90, 10%, 11%,

614 0.92, and 2 h, respectively. All evaluation indices improved after parameter optimization, with

615 the average values of the Nash–Sutcliffe coefficient, correlation coefficient, and water balance

616 coefficient increasing by 0.13, 0.16, and 0.23, respectively. The average values of the relative

617 flow process error, flood peak error, and peak time error decreased by 15%, 14%, and 3 h,

618 respectively. These reasonable flood simulation results confirmed that parameter optimization

619 by the ICPSO algorithm was necessary and effective for the QMG model.

620 **5 Discussion**

621 **5.1 Model evaluation**

622 Compared with the overall flow process simulation shown in Figure 6, each flood process was

623 better simulated by the QMG model (Fig. 7). This was because the main consideration of the

624 QMG model was the calculation of the flood process and the correlation algorithm of the dry

625 season runoff was not sufficiently described. For example, equations (12)–(15) represent the

626 flood convergence algorithm. As a result, the model is not good at simulating other flow

627 processes, such as dry season runoff, leading to a low accuracy in the overall flow process. The

628 next phase of our research will focus on refining the algorithm related to dry season runoff and

629 improving the comprehensive performance of the model.

630 **5.2 Parameter sensitivity analysis**

631 The parameter sensitivity results in Table 2 show that the rainfall infiltration coefficient in the

632 QMG model was the most sensitive parameter. This was the key to determining the generation

633 of excess infiltration surface runoff and separating surface runoff from subsurface runoff. If the

634 rainfall infiltration coefficient was greater than the infiltration capacity, excess infiltration

635 surface runoff was generated on the exposed karst landforms; otherwise, all rainfall would

636 infiltrate to meet the water deficit in the vadose zone and then continue to seep into the

637 underground river system, eventually flowing out of the basin through the underground river

638 outlet. The confluence modes of surface runoff and underground runoff were completely

639 different, resulting in a large difference in the simulated flow results. Therefore, the rainfall

640 infiltration coefficient had the greatest impact on the final flood simulation results.

641   Other highly sensitive parameters, such as the rock permeability coefficient, rock porosity

642 and specific yield, were used as the basis for dividing between slow flow in karst fissures and

643 rapid flow in conduits. The division of slow and rapid flows also had a great impact on the

644 discharge at the outlet of the basin. Slow flow plays an important role in water storage in a karst

645 aquifer and is very important for the replenishment of river base flow in the dry season. Rapid

646 flow in large conduit systems dominates flood runoff and is the main component of the flood

647 water volume in the flood season.

648   Parameters related to the soil water content, including the saturated water content, field

649 capacity and thickness, were sensitive parameters and had a strong influence on the flood

650 simulation results. This is because the soil moisture content prior to flooding affects how flood

651 flows rise and when peaks occur. If the soil is already very wet or even saturated before flooding,

652 a flood rises quickly to a peak, and the process line of the flood peak flow is sharp and thin.

653 This type of flood process forms easily and can lead to disaster-causing flood events. In contrast,

654 if the soil in the basin is very dry before flooding, the rainfall first counteracts the water shortage

655 of the vadose zone, and after this zone is replenished, the rainfall infiltrates into the underground

656 river. The flood peak of the river basin outlet is therefore delayed.

657   The flow direction, slope and the soil coefficient were moderately sensitive parameters.

658 They had a specific influence on the flood simulation results, but the influence was not as great

659 as that of the highly sensitive and sensitive parameters. The channel roughness and the

660 evaporation coefficient were insensitive parameters. The amount of water lost by

661 evapotranspiration is a very small in part of the total flood water, and it was therefore the least

662 sensitive parameter in the QMG model.

663 **5.3 Assessment and reduction of uncertainty**

664 In general, the uncertainty in model simulation is due mainly to three aspects of the model: (i)

665 the uncertainty of its input data, (ii) the uncertainty of its structure and algorithm and (iii) the

666 uncertainty of its parameters. In the practical application of a hydrological model, these three

667 uncertainties are usually interwoven, which leads to the overall uncertainty of the final

668 simulation results (Krzysztofowicz, 2014). Therefore, the present study focused on the

669 uncertainties in the input data, the model structure and the parameters to reduce the overall

670 uncertainty of the simulation results.

671   First, the input data—mainly rainfall-runoff data and hydrogeological data—were

672 preprocessed, which substantially reduced their uncertainty. Second, we simplified the structure

673 of the QMG model, which is reflected in the fact that it has only two layers of spatial structure

674 in the horizontal and vertical directions. This relatively simple structure greatly reduced the

675 model structure-related uncertainty. In contrast, the underground structure of our previous

676 Karst–Liuxihe model (Li et al., 2021) has five layers, which leads to great uncertainty. Third,

677 appropriate algorithms for runoff generation and confluence were selected. Different models

678 were designed for different purposes, which led to great differences in the algorithms used. In

679 the QMG model, most of the rainfall-runoff algorithms used have been validated against the

680 research results of others, and some of them were improved to suit karst flood simulation and

681 prediction by the QMG model. For example, the algorithm for the generation of excess

682 infiltration runoff [Eq. (2)] represented an improvement over the version used in the Liuxihe

683 model (Chen, 2009, 2018; Li et al., 2020). Finally, the algorithm for parameter optimization

684 was improved. Considering that the standard PSO algorithm tends to converge locally, this

685 study developed the ICPSO for parameter optimization by adding chaotic perturbation factors.

686 The flood simulation results after parameter optimization were much better than those of the

687 initial model parameters (Figs. 6 and 7 and Tables 2 and 3), which indicates that parameter

688 optimization is necessary for a distributed hydrological model and can reduce the uncertainty

689 of the model parameters.

690 **6 Conclusions**

691 This study proposed a new distributed physically based hydrological model, i.e., the QMG

692 model, to accurately simulate floods in karst trough and valley landforms. The main conclusions

693 of this paper are as follows.

694 1) The QMG model has a high application potential for karst hydrology simulations. Other

695 distributed hydrological models usually have multiple structures, resulting in the need for a

large amount of data to build models in karst areas (Kraller et al., 2014). The QMG model has only a double-layer structure, with a clear physical meaning, and a small amount of basic data is needed to build the model in karst areas, such as some necessary hydrogeological data. For example, the distribution and flow direction of underground rivers is needed, which can be inferred from a tracer test, leading to a low modelling cost. There are fewer parameters in the QMG model than in other distributed hydrological models, with only 10 parameters that need to be calibrated.

2) The flood simulation after parameter optimization was much better than the simulation using the initial model parameters. After parameter optimization, the average values of the Nash–Sutcliffe coefficient, correlation coefficient and water balance coefficient increased by 0.13, 0.16 and 0.23, respectively, while the average relative flow process error, flood peak error and peak time error decreased by 15%, 14% and 3 h, respectively. Parameter optimization is necessary for a distributed hydrological model, and the improvement of the ICPSO algorithm in this study was an effective way to achieve this.

3) In the QMG model, the rainfall infiltration coefficient I_c, rock permeability coefficient K, rock porosity R_p and the parameters related to the soil water content were sensitive parameters. The order of the parameter sensitivity values was as follows: infiltration coefficient > permeability coefficient > rock porosity > specific yield > saturated water content > field capacity > flow direction > thickness > slope > soil coefficient > channel roughness > evaporation coefficient.

The QMG model is suitable for karst trough and valley landforms such as the current study area, where the topography is conducive to the spread of flood water. Whether this model is applicable to the karst areas of other landforms still needs to be verified in future studies. In addition, the basin area is very small, while the hydrological similarity between different small basin areas varies greatly (Kong and Rui, 2003). The size of the area to be modelled has a great influence on the choice of model spatial resolution (Chen et al., 2017). Therefore, whether the QMG model is suitable for flood prediction in large karst basins needs to be determined.

Model development.

The QMG model presented in this study uses Visual Basic language programming. The general framework of the model and the algorithm consist of three parts: the modelling approach, the algorithm of rainfall-runoff generation and confluence, and the parameter optimization algorithm. As this model is a free and open-source hydrological modelling program (QMG model-V1.0), we provide all modelling packages, including the model code, installation package, simulation data package and user manual, free of charge. It is important to note that the model we provide is only for scientific research purposes and should not be used for any commercial purposes. Creative Commons Attribution 4.0 International.

The model installation program can be downloaded from ZENODO, cite as JI LI. (2021, June 16). QMG model-V1.0. Zenodo. http://doi.org/10.5281/zenodo.4964701, and http://doi.org/10.5281/zenodo.4964697 (registration required). The user manual can be downloaded from http://doi.org/10.5281/zenodo.4964754.

Code availability.

All codes for the QMG model-V1.0 in this paper are available for free, and the code can be downloaded from ZENODO. Cite as JI LI. (2021, June 16). QMG model-V1.0 code (Version v1.0). Zenodo. http://doi.org/10.5281/zenodo.4964709 (registration required).

Data availability.

All data used in this paper are available, findable, accessible, interoperable, and reusable. The simulation data and modelling data package can be downloaded from http://doi.org/10.5281/zenodo.4964727. The DEM was downloaded from the Shuttle Radar Topography Mission database at http://srtm.csi.cgiar.org. The land use-type data were downloaded from http://landcover.usgs.gov, and the soil-type data were downloaded from http://www.isric.org. These data were last accessed on 15 October 2020.

Author contributions. JIL was responsible for the calculations and writing of the whole paper.

DY helped conceive the structure of the model. ZF and JL provided significant assistance in the

English translation of the paper. MM provided flow data of the study area.

Competing interests.

The authors declare that they have no conflicts of interest.

Acknowledgements.

This study was supported by the National Natural Science Foundation of China (41830648), National Science Foundation for Young Scientists of China (42101031), Fundamental Research Funds for the Central Universities (SWU-KQ22001), Chongqing Natural Science Foundation

756 (cstc2021jcyj-msxm0007), and the Chongqing Education Commission Science and Technology

757 Research Foundation (KJQN202100201), drought monitoring, analysing and early warning

758 of typical prone-to-drought areas of Chongqing (20C00183), and the Open Project Program of

759 Guangxi Key Science and Technology Innovation Base on Karst Dynamics (KDL & Guangxi

760 202009, KDL & Guangxi 202012).

761 **References**

762 Abbott, M. B., Bathurst, J. C., Cunge, J. A., O'Connell, P. E., and Rasmussen, J.: An

763   Introduction to the European HydrologicSystem-System Hydrologue Europeen, 'SHE', a:

764   History and Philosophy of a Physically-based, Distributed Modelling System,J. Hydrol.,

765   87, 45–59, 1986a.

766 Abbott, M. B., Bathurst, J. C., Cunge, J. A., O'Connell, P. E., and Rasmussen, J.: An

767   Introduction to the European Hydrologic System-System Hydrologue Europeen, 'SHE', b:

768   Structure of a Physically based, distributed modeling System, J. Hydrol., 87,61–77, 1986b.

769 Ambroise, B., Beven, K., and Freer, J.: Toward a generalization of the TOPMODEL concepts:

770   Topographic indices of hydrologic similarity. Water Resources Research, 32, 2135-2145,

771   1996.

772 Atkinson, T.C.: Diffuse flow and conduit flow in limestone terrain in the Mendip Hills,

773   Somerset (Great Britain). Journal of Hydrology, 35, 93-110, 1977.

774   https://doi.org/10.1016/0022-1694(77)90079-8

775 Berry, R.A., Saurel, R., and Lemetayer, O.: The discrete equation method (DEM) for fully

776   compressible, two-phase flows in ducts of spatially varying cross-section. Nuclear

777   Engineering & Design, 240(11), 3797-3818, 2010.

778 Beven, K., and Binley, A.: The future of distributed models: Model calibration and uncertainty

779   prediction. Hydrological Processes, 6, 279-298, 2006.

780 Birk, S., Geyer, T., Liedl, R., and Sauter, M.: Process-based interpretation of tracer tests in

781   carbonate aquifers. Ground Water, 43(3), 381-388, 2005.

782 Bittner, D., Parente, M.T., Mattis, S., Wohlmuth, B., and Chiogna, G.: Identifying relevant

783   hydrological and catchment properties in active subspaces: An inference study of a lumped

784   karst aquifer model. ADVANCES IN WATER RESOURCES,135,550-560, 2020

785   doi: 10.1016/j.advwatres.2019.103472

786 Blansett, K. L., and Hamlett, J. M.: Challenges of Stormwater Modeling for Urbanized Karst

Basins. Pittsburgh, Pennsylvania, an ASABE Meeting Presentation, Paper Number: 1009274, 2010. doi:10.13031/2013.29840

Blansett, K. L.: Flow, water quality, and SWMM model analysis for five urban karst basins.. (Doctoral dissertation). The Pennsylvania State University, USA, 2011.

Bonacci, O., Ljubenkov, I., and Roje-Bonacci, T.: Karst flash floods: an example from the Dinaric karst Croatia. Nat. Hazards Earth Syst. Sci. 6, 195–203, 2006.

Chang, Y., and Liu, L.: A review of hydrological models in karst areas. Engineering investigation, 43,37-44, 2015.

Chang, Y., Hartmann, A., Liu, L., Jiang, G., and Wu, J.: Identifying more realistic model structures by electrical conductivity observations of the karst spring. Water Resources Research, 2021. doi: 10.1029/2020WR028587

Chen, G.M., Jia, J.Y., and Han, Q.: Research on inertia weight reduction strategy of Particle Swarm optimization algorithm. Journal of Xi'an Jiaotong University, 40(1),53-56, 2006.

Choi, J., Harvey, J. W., and Conklin, M. H.: Use of multi-parameter sensitivity analysis to determine relative importance of factors influencing natural attenuation of mining contaminants. the Toxic Substances Hydrology Program Meeting, Charleston,South Carolina, 1999.

Chen, Y. B.: Liuxihe Model, China Science and Technology Press, Beijing, China, 2009.

Chen, Y., Li, J., and Xu, H.: Improving flood forecasting capability of physically based distributed hydrological models by parameter optimization. Hydrol. Earth Syst. Sci. 20, 375-392, 2016. https://doi.org/10.5194/hess-20-375-2016

Chen, Y., Li, J., Wang, H., Qin, J., and Dong, L.: Large watershed flood forecasting with high-resolution distributed hydrological model. Hydrol. Earth Syst. Sci. 21, 735-749, 2017. https://doi.org/10.5194/hess-21-735-2017

Chen, Y.: Distributed Hydrological Models. Springer Berlin Heidelberg, Berlin, Germany. 2018. https://doi.org/10.1007/978-3-642-40457-3_23-1

813 Dewandel, B., Lachassagne, P., Bakalowicz, M., Weng, P., and Malki, A.A.: Evaluation of
814   aquifer thickness by analysing recession hydrographs. Application to the Oman ophiolite
815   hard-rock aquifer. Journal of Hydrology, 274,248-269, 2003.

816 Dubois, E., Doummar, J., Séverin Pistre, S., and Larocque, M.: Calibration of a lumped karst
817   system model and application to the Qachqouch karst spring (Lebanon) under climate
818   change conditions. Hydrol. Earth Syst. Sci., 24, 4275-4290, 2020.
819   https://doi.org/10.5194/hess-24-4275-2020

820 Doummar, J., Sauter, M., and Geyer, T.: Simulation of flow processes in a large scale karst
821   system with an integrated catchment model (MIKE SHE) – identification of relevant
822   parameters influencing spring discharge. Journal of Hydrology, 426-427, 112-123, 2012.

823 Epting, J., Page, R.M., and Auckenthaler, A.: Process-based monitoring and modeling of Karst
824   springs–Linking intrinsic to specific vulnerability. Science of the Total Environment, 625,
825   403-415, 2018.

826 Fleury, P., Plagnes, V., and Bakalowicz, M.: Modelling of the functioning of karst aquifers with
827   a reservoir model: Application to Fontaine de Vaucluse (South of France). Journal of
828   Hydrology, 345,38-49, 2007b. http://dx.doi.org/10.1016/j.jhydrol.2007.07.014

829 Ford, D. C., and Williams, P.W.: Karst geomorphology and hydrology. Wiley, Chichester,
830   England, 2007.

831 Gang, L., Tong, F.G., and Bin,T.: A Finite Element Model for Simulating Surface Runoff and
832   Unsaturated Seepage Flow in the Shallow Subsurface. Hydrological Processes, 6,102-120,
833   2019. doi: 10.1002/hyp.13564

834 Gautama, R.S., Notosiswoyo, S., Zen, M.T., and Kusumayudha, S. B.: Mathematical model of
835   fractal conduits flow mechanics in the gunungsewu karst area, yogyakarta special region,
836   indonesia. International Journal of Hydrology Science and Technology, 1(1), 1, 2021. doi:
837   10.1504/IJHST.2021.10035255

838 Geyer, T., Birk, S., Liedl, R., and Sauter, M.: Quantification of temporal distribution of recharge
839   in karst systems from spring hydrographs. Journal of Hydrology, 348(30), 452-463, 2008.

Gou, P.F., Jiang, Y.J., Hu, Z.Y., Pu, J.B., and Yang, P.H.: A study of the variations in hydrology and hydrochemistry under the condition of a storm in a typical karst subterranean stream. HYDROGEOLOGY&ENGINEERING GEOLOGY,37(5),20-25, 2010.

Guila, J. F., Samper, J., Belén, B., Paloma, G., and Montenegro, L.: Reactive transport model of gypsum karstification in physically and chemically heterogeneous fractured media. Energies, 15, 1-29, 2022.

Gutierrez, F.: Hazards associated with karst. In: Alcantara, I. & A. Goudie (Eds.), Geomorphological Hazards and Disaster Prevention. Cambridge University Press, Cambridge, 161–175, 2010.

Gutierrez, F., Parise, M., D' Waele, J., and Jourde, H.: A review on natural and human-induced geohazards and impacts in karst. Earth Science Reviews, 138, 61-88, 2014.

Hartmann, A., and Baker, A.: Progress in the hydrologic simulation of time variant of karst systems-Exemplified at a karst spring in Southern Spain. Advances in Water Resources, 54,149-160, 2013.

Hartmann, A., Goldscheider, N., Wagener, T., Lange, J., and Weiler, M.: Karst water resources in a changing world: Review of hydrological modeling approaches. Reviews of Geophysics 52: 218-242, 2014a. doi: 10.1002/2013RG000443

Hartmann, A., and Baker, A.: Modelling karst vadose zone hydrology and its relevance for paleoclimate reconstruction. Earth-Science Reviews, 172, 178-192, 2017.

Hartmann, A.: Experiences in calibrating and evaluating lumped karst hydrological models. London: Geological Society, Special Publications, 2018.

Jamal, M. S., and Awotunde, A.A.: Darcy model with optimized permeability distribution (dmopd) approach for simulating two-phase flow in karst reservoirs. Journal of Petroleum Exploration and Production Technology, 2022. doi:10.1007/S13202-021-01385-X

Jourde, H., Roesch, A., Guinot, V., and Bailly-Comte, V.: Dynamics and contribution of karst groundwater to surface flow during Mediterranean flood. Environ. Geol. 51 (5),

866   725–730, 2007.

867   Jourde, H., Lafare, A., Mazzilli, N., Belaud, G., Neppel, L., Doerfliger, N., and Cernesson, F.:

868   Flash flood mitigation as a positive consequence of anthropogenic forcings on the

869   groundwater resource in a karst catchment. Environ. Earth Sci. 71, 573–583,2014.

870   Jukić, D., and Denić-Jukić, V.: Groundwater balance estimation in karst by using a conceptual

871   rainfall–runoff model. Journal of Hydrology, 373, 302-315, 2009.

872   http://dx.doi.org/10.1016/j.jhydrol.2009.04.035

873   Kong, F.Z., and Rui, X.F.: Hydrological similarity of catchments based on topography.

874   GEOGRAPHICAL RESEARCH, (06), 709-715, 2003.

875   Kovács, A., and Sauter, M.: Modelling karst hydrodynamics. In: Goldscheider N, Drew D (eds)

876   Methods in karst hydrogeology, IAH international contributions to hydrogeology; 26,264

877   p, 2007.

878   Kovács, A., and Perrochet, P.: A quantitative approach to spring hydrograph decomposition.

879   Journal of Hydrology, 352, 16-29, 2008. http://dx.doi.org/10.1016/j.jhydrol.2007.12.009

880   Kurtulus, B., and Razack, M.: Evaluation of the ability of an artificial neural network model to

881   simulate the input-output responses of a large karstic aquifer: the la rochefoucauld aquifer

882   (charente, france). Hydrogeology Journal, 15(2), 241-254, 2007.

883   Krzysztofowicz, R., and Kelly, K.: Hydrologic uncertainty processor for probabilistic river

884   stage forecasting. Water Resources Research, 36(11),3265-3277, 2000.

885   Krzysztofowicz, R.: Probabilistic flood forecast:Exact and approximate predictive

886   distributions. Journal of Hydrology, 517(1), 643-651, 2014.

887   Kraller, G., Warscher, M., Strasser, U., Kunstmann, H., and Franz, H.: Distributed hydrological

888   modeling and model adaption in high alpine karst at regional scale (berchtesgaden alps,

889   germany). Springer International Publishing Switzerland, 2014.

890   https://doi.org/10.1007/978-3-319-06139-9_8

891   Ladouche, B., Marechal, J. C., and Dorfliger, N.: Semi-distributed lumped model of a karst

892   system under active management. Journal of Hydrology, 509,215-230, 2014.

Li, J., Chen, Y., Wang, H., Qin, J., Li, J., and Chiao, S.: Extending flood forecasting lead time in a large basin by coupling WRF QPF with a distributed hydrological model, Hydrol. Earth Syst. Sci. 21, 1279–1294, 2017. https://doi.org/10.5194/hess-21-1279-2017

Li, J., Yuan, D., Liu, J., Jiang, Y., Chen, Y., Hsu, K. L., and Sorooshian, S.: Predicting floods in a large karst river basin by coupling PERSIANN-CCS QPEs with a physically based distributed hydrological model. Hydrol. Earth Syst. Sci. 23, 1505-1532, 2019. https://doi.org/10.5194/hess-23-1505-2019

Li, J., Hong, A., Yuan, D., Jiang,Y., Deng,S., Cao,C., and Liu, J.: A new distributed karst-tunnel hydrological model and tunnel hydrological effect simulations. Journal of Hydrology, 593, 125639, 2020. https://doi.org/10.1016/j.jhydrol.2020.125639

Li, J., Hong, A., Yuan, D., Jiang,Y., Zhang,Y., Deng,S., Cao,C., Liu, J., and Chen,Y.: Elaborate Simulations and Forecasting of the Effects of Urbanization on Karst Flood Events Using the Improved Karst-Liuxihe Model.CATENA,197,104990, 2021. https://doi.org/10.1016/j.catena.2020.104990

Liedl, R.., Sauter, M., Huckinghaus, D., Clemens, T., and Teutsch, G.: Simulation of the development of karst aquifers using a coupled continuum pipe flow model. Water Resources Research, 39, 50-57, 2003.

Liu, X., Jiang, Y.J., Ye, M.Y., Yang, P.H., Hu, Z.Y., and Li, Y.Q.: Study on hydrologic regime of underground river in typical karst valley- A case study on the Qingmuguan subterranean stream in Chongqing. CARSOLOGICA SINICA, 28(2),149-154, 2009.

Lu, D. B., Shi, Z. T., Gu, S. X., and Zeng, J. J.: Application of Hydrological Model in the Karst Area. Water-saving irrigation.11, 31-34, 2013. doi:1007-4929(2013)11-031-04

Martinotti, M.E., Pisano, L., Marchesini, I., Rossi, M., Peruccacci, S., Brunetti, M.T., Melillo, M.,Amoruso, G., Loiacono, P., Vennari, C., Vessia, G., Trabace, M., Parise, M., and Guzzetti, F.: Landslides, floods and sinkholes in a karst environment: the 1–6 September 2014 Gargano event, southern Italy. Natural Hazards and Earth System Sciences, 17, 467-480, 2017.

920 Masciopinto, C., Passarella, G., Caputo, M.C., Masciale, R, and Carlo, L.D.: Hydrogeological

921 models of water flow and pollutant transport in karstic and fractured reservoirs. Water

922 Resources Research, 57, 2021. doi: 10.1029/2021WR029969

923 Meng, H.H., Wang, N.C., Su, W.C., and Huo, Y.: Modeling and application of karst semi-

924 distributed hydrological model based on sinkholes. SCIENTIA GEOGRAPHICA SINICA,

925 5, 550-554, 2009. doi: 10.3969/j.issn.1000-0690.2009.04.014

926 Meng, H.H., and Wang, N.C.: Advances in the study of hydrological models in karst basin.

927 Progress in Geography, 29,1311-1318, 2010.

928 Pan, H.Y.: Hydrological model and application in karst watersheds. China University of

929 Geosciences. Doctoral Dissertation, Wuhan, China, 2014.

930 Parise, M.: Hazards in karst, Proceedings Int. Conf. "Sustainability of the karst environment.

931 Dinaric karst and other karst regions", IHP-Unesco, Series on Groundwater,2, 155-162,

932 2010.

933 Peterson, E.W., and Wicks, C. M.: Assessing the importance of conduit geometry and physical

934 parameters in karst systems using the storm water management model (SWMM). Journal

935 of Hydrology, 329, 1-2, 294-305, 2006.

936 Peterson, J.R., and Hamlett, J.M.: Hydrologic calibration of the SWAT model in a basin

937 containing fragipan soils. JAWRA Journal of the American Water Resources Association,

938 1998. doi: 10.1111/j.1752-1688.1998. tb00952.x

939 Petrie, R., Denvil, S., Ames, S.,et al.: Coordinating an operational data distribution network for

940 CMIP6 data, Geosci. Model Dev., 14, 629–644, 2021. https://doi.org/10.5194/gmd-14-

941 629-2021

942 Qin, J.G., and Jiang, Y.P.: A review of numerical simulation methods for CFP pipeline flow.

943 Groundwater. 3, 98-100, 2014.

944 Reimann, T., Melissa, E., and Hill.: Modflow-cfp: a new conduit flow process for modflow–

945 2005. Ground Water,47(3),321-325, 2009. doi:10.1111/j.1745-6584.2009.00561.x

946 Ren, Q.W.: Water Quantity Evaluation Methodology Based on Modified SWAT Hydrological

947   Modeling in Southwest Karst Area, China University of Geoscience, Wuhan, China, 2006.

948   Shoemaker, W.B., Cunningham, K.J., and Kuniansky, E.L.: Effects of turbulence on hydraulic

949   heads and parameter sensitivities in preferential groundwater flow layers. Water Resources

950   Research, 44, 34-50, 2008. doi: 10.1029/2007WR006601

951   Suo, L.T., Wan, J.W., and Lu, X.W.: Improvement and application of TOPMODEL in karst

952   region. Carsologica Sinica, 26(1), 67-70, 2007.

953   Teixeiraparente, M., Bittner, D., Mattis, S.A., Chiogna, G., and Wohlmuth, B.: Bayesian

954   calibration and sensitivity analysis for a karst aquifer model using active subspaces. Water

955   Resources Research, 55, 342-356, 2019. doi: 10.1029/2019WR024739

956   White, W.B.: Karst hydrology: recent developments and open questions. Eng. Geol. 65, 85–

957   105, 2002.

958   Williams, P.W.: The role of the epikarst in karst and cave hydrogeology: a review. Int. J. Speleol.

959   37, 1–10, 2008.

960   Williams, P. W.: Book Review: Methods in Karst Hydrogeology, Nico Goldscheider and David

961   Drew (eds). Hydrogeology Journal, 17,1025-1025, 2009.

962   Worthington, S., Ford, D., and Beddows, P.: Porosity and permeability enhancement in

963   unconfined carbonate aquifers as a result of solution. Speleogenesis: evolution of karst

964   aquifers, 2000.

965   Yang, P. H., Luo, J.Y., Peng, W., Xia, K.S., and Lin, Y.S.: Application of online technique in

966   tracer test-A case in Qingmuguan subterranean river system, Chongqing, China.

967   CARSOLOGICA SINICA, 27(3),215-220, 2008.

968   Yu, D., Yin, J., Wilby, R.L., Stuart, N. L., Jeroen, C., Lin, N., Liu, M., Yuan, H., Chen, J.,

969   Christel, P., Guan, M., Avinoam, B., Charlie, W. D., Tang, X., Yu, L., and Xu, S.:

970   Disruption of emergency response to vulnerable populations during floods. Nature

971   Sustainability, 3, 728–736, 2020. https://doi.org/10.1038/s41893-020-0516-7

972   Yu, Q., Yang,. P.H., Yu, Z.L., Chen, X.B., and Wu, H.: Dominant factors controlling

973   hydrochemical variationg of karst underground river in different period, Qingmuguan,
974   Chongqing. CARSOLOGICA SINICA, 35(2),134-143, 2016

975   Zhang, H.: Characterization of a multi-layer karst aquifer through analysis of tidal fluctuation.
976   Journal of Hydrology, 601, 126677, 2021. doi: 10.1016/j.jhydrol.2021.126677

977   Zhang, Q.: Assesment on the intrinsic vulnerability of karst groundwater source in the
978   Qingmuguan karst valley. CARSOLOGICA SINICA, 31(1),67-73, 2012.Zhu, C., and Li,
979   Y.: Long-Term Hydrological Impacts of Land Use/Land Cover Change From 1984 to 2010
980   in the Little River Basin, Tennessee. International Soil and Water Conservation Research,
981   2(2), 11-21, 2014.

982 **Tables**

983 Table 1 Parameters of the QMG model.

Parameter	Variable name	Physical property
Infiltration coefficient	I_c	Meteorology
Evaporation coefficient	λ	Vegetation cover
Soil thickness	h	Karst aquifer
Soil coefficient	S_b	Soil type
Saturated water content	S_c	Soil type
Rock porosity	R_p	Karst aquifer
Field capacity	F_c	Soil type
Permeability coefficient	K	Karst aquifer
Flow direction	F_d	Landform
Slope	S_0	Landform
Specific yield	S_y	Karst aquifer
Channel roughness	n	Landform

984 Table 2 Parametric sensitivity results in the QMG model.

I_c	λ	h	S_b	S_c	S_y	F_d	S_0	R_p	F_c	K	n
0.92	0.24	0.71	0.58	0.8	0.83	0.74	0.68	0.86	0.78	0.89	0.36

985 Table 3 Flood simulation evaluation indices without and with parametric optimization.

Parameter optimization	Parameter type	Nash–Sutcliffe coefficient	Correlation coefficient	Relative flow process error/%	Flood peak error/%	Water balance coefficient	Peak time error (hours)
calibration period	initial	0.82	0.77	24	29	0.82	4
	optimized	0.91	0.94	14	12	0.95	2
validation period	initial	0.79	0.71	29	32	0.77	6
	optimized	0.88	0.87	18	16	0.92	3
average value	initial	0.81	0.74	27	31	0.8	5
	optimized	0.9	0.91	16	14	0.94	3

986 Table 4 Flood simulation indices for model validation.

Flood	Parameter type	Nash–Sutcliffe coefficient	Correlation coefficient	Relative flow process error/%	Flood peak error/%	Water balance coefficient	Peak time error/(hours)
2017042408	initial	0.77	0.7	28	29	0.71	-5
	optimized	0.95	0.89	11	15	0.88	-2
2017050816	initial	0.78	0.71	19	19	0.76	-4
	optimized	0.92	0.88	11	9	0.94	-2
2017061518	initial	0.76	0.6	25	32	0.63	-5

ID							
	optimized	0.91	0.93	12	11	0.95	-3
2017071015	initial	0.78	0.82	25	37	0.64	-4
	optimized	0.92	0.87	8	7	0.94	-2
2017091512	initial	0.81	0.62	21	16	0.78	-5
	optimized	0.9	0.92	13	10	0.9	-4
2017100815	initial	0.75	0.68	30	26	0.62	-2
	optimized	0.94	0.86	11	15	0.92	-1
2018052016	initial	0.78	0.68	25	21	0.67	5
	optimized	0.91	0.93	10	13	0.94	2
2018060815	initial	0.82	0.79	27	22	0.69	-6
	optimized	0.9	0.92	11	12	0.93	-4
2018071212	initial	0.84	0.75	26	24	0.61	5
	optimized	0.91	0.88	8	15	0.92	3
2018081512	initial	0.71	0.78	26	24	0.78	-4
	optimized	0.89	0.94	12	11	0.89	-3
2018090516	initial	0.85	0.68	28	23	0.68	-5
	optimized	0.93	0.87	12	10	0.92	-2
2018092514	initial	0.79	0.78	23	19	0.59	5
	optimized	0.88	0.88	9	11	0.89	2
2018101208	initial	0.78	0.81	28	25	0.63	5
	optimized	0.92	0.94	11	10	0.94	2
2018111208	initial	0.79	0.81	25	24	0.65	-6
	optimized	0.94	0.86	13	12	0.92	-2
2019042512	initial	0.78	0.8	26	36	0.8	5
	optimized	0.89	0.94	9	16	0.93	2
2019051513	initial	0.84	0.77	32	27	0.79	4
	optimized	0.91	0.88	9	13	0.95	2
2019052516	initial	0.74	0.75	29	26	0.63	-5
	optimized	0.92	0.86	7	15	0.96	-2
2019060518	initial	0.85	0.83	28	25	0.78	-4
	optimized	0.95	0.96	10	12	0.92	-2
average value	initial	0.79	0.74	26	25	0.69	5
	optimized	0.92	0.9	10	11	0.92	2

Figures
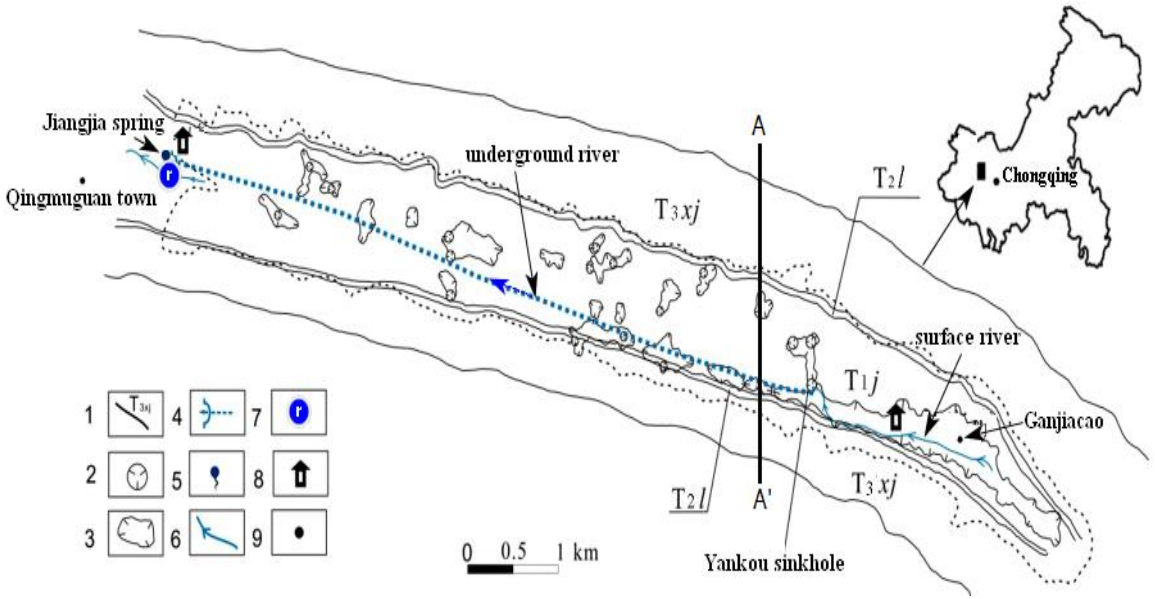
1- stratigraphic boundary, 2-sinkhole, 3- karst depression, 4- underground river, 5- karst spring, 6-surface river, 7-river gauge, 8- rain gauge, and 9- geographical name

a. Qingmuguan karst basin (modified from Yu et al., 2016)
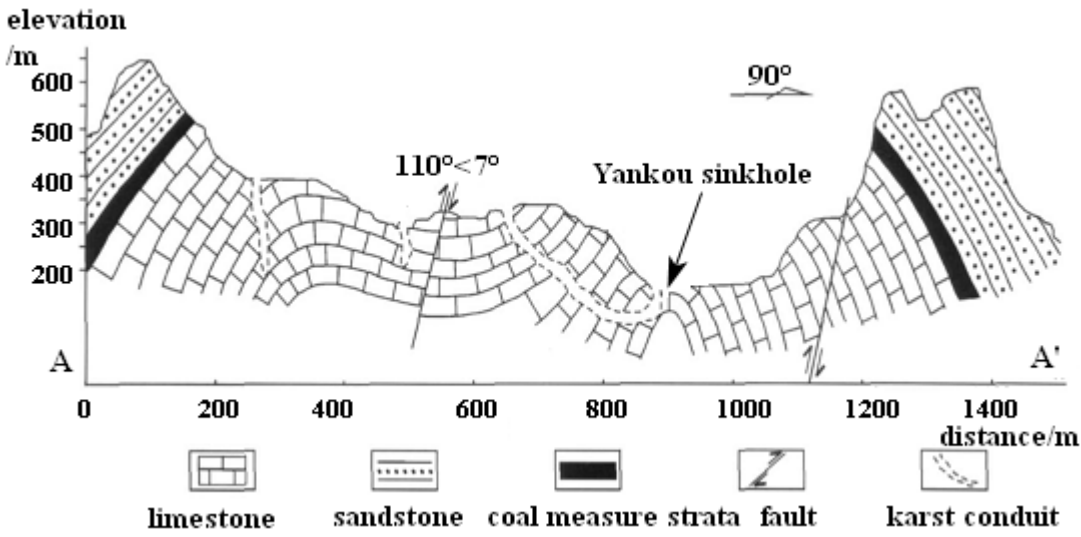
b. Lithologic cross-section of the Yankou sinkhole/AA' (modified from Zhang, 2012)

994
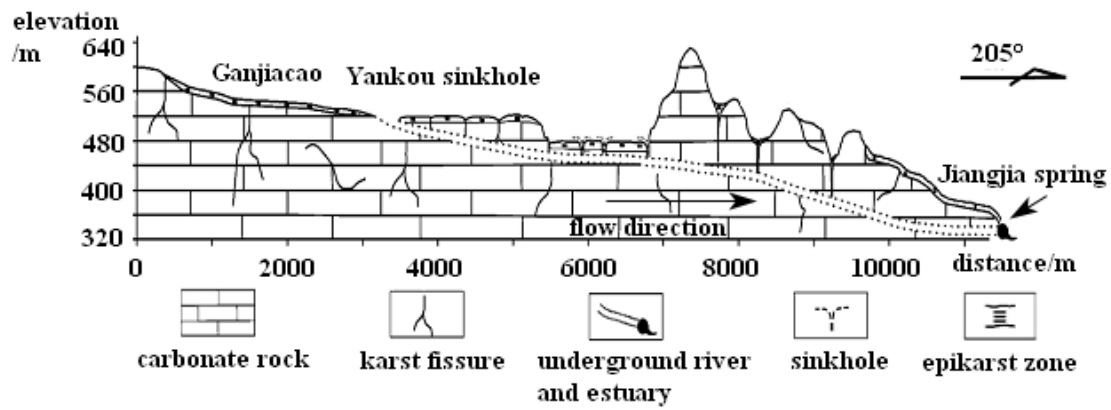
995   c. Longitudinal profile of the study area (modified from Yang et al., 2008)
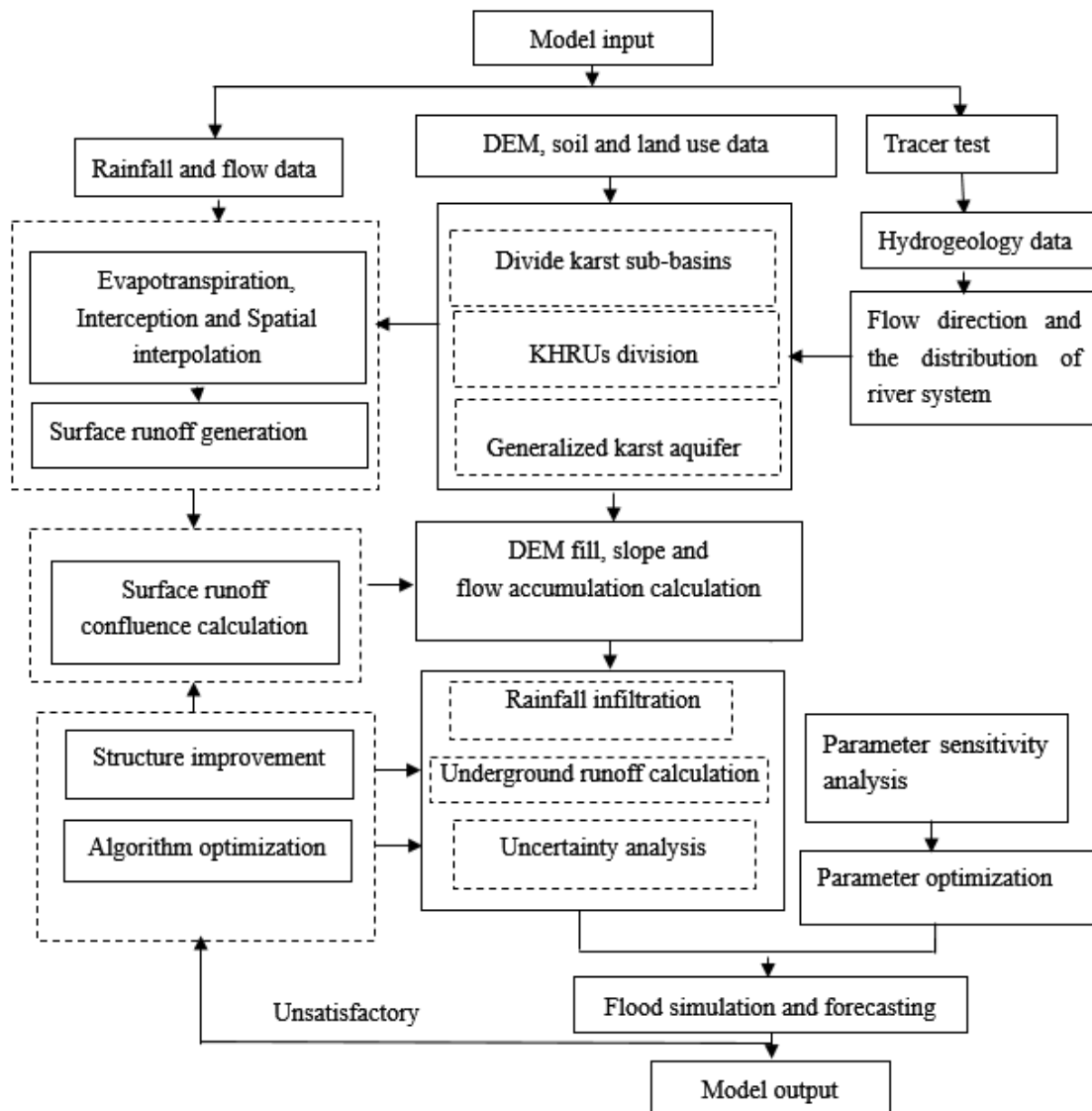
996   Figure 1 The Qingmuguan karst basin.

```
                            ┌──────────────────┐
                            │   Model input    │
                            └──────────────────┘

┌─────────────────────┐  ┌──────────────────────────┐  ┌──────────────────┐
│ Rainfall and flow   │  │ DEM, soil and land use   │  │   Tracer test    │
│       data          │  │          data            │  │                  │
└─────────────────────┘  └──────────────────────────┘  └──────────────────┘

                         ┌ ─ ─ ─ ─ ─ ─ ─ ─ ─ ─ ─ ─ ┐    ┌──────────────────┐
┌─────────────────────┐  │  Divide karst sub-basins │    │ Hydrogeology data│
│ Evapotranspiration, │  └ ─ ─ ─ ─ ─ ─ ─ ─ ─ ─ ─ ─ ┘    └──────────────────┘
│ Interception and    │  ┌ ─ ─ ─ ─ ─ ─ ─ ─ ─ ─ ─ ─ ┐    ┌──────────────────┐
│ Spatial             │  │     KHRUs division       │    │ Flow direction   │
│ interpolation       │  └ ─ ─ ─ ─ ─ ─ ─ ─ ─ ─ ─ ─ ┘    │ and the          │
├─────────────────────┤  ┌ ─ ─ ─ ─ ─ ─ ─ ─ ─ ─ ─ ─ ┐    │ distribution of  │
│ Surface runoff      │  │  Generalized karst       │    │ river system     │
│ generation          │  │  aquifer                 │    └──────────────────┘
└─────────────────────┘  └ ─ ─ ─ ─ ─ ─ ─ ─ ─ ─ ─ ─ ┘

┌─────────────────────┐  ┌──────────────────────────┐
│ Surface runoff      │  │ DEM fill, slope and      │
│ confluence          │  │ flow accumulation        │
│ calculation         │  │ calculation              │
└─────────────────────┘  └──────────────────────────┘

┌─────────────────────┐  ┌ ─ ─ ─ ─ ─ ─ ─ ─ ─ ─ ─ ─ ┐   ┌──────────────────┐
│ Structure           │  │    Rainfall infiltration │   │ Parameter        │
│ improvement         │  └ ─ ─ ─ ─ ─ ─ ─ ─ ─ ─ ─ ─ ┘   │ sensitivity      │
├─────────────────────┤  ┌ ─ ─ ─ ─ ─ ─ ─ ─ ─ ─ ─ ─ ┐   │ analysis         │
│ Algorithm           │  │ Underground runoff       │   └──────────────────┘
│ optimization        │  │ calculation              │   ┌──────────────────┐
└─────────────────────┘  └ ─ ─ ─ ─ ─ ─ ─ ─ ─ ─ ─ ─ ┘   │ Parameter        │
                         ┌ ─ ─ ─ ─ ─ ─ ─ ─ ─ ─ ─ ─ ┐   │ optimization     │
                         │    Uncertainty analysis  │   └──────────────────┘
                         └ ─ ─ ─ ─ ─ ─ ─ ─ ─ ─ ─ ─ ┘

           Unsatisfactory     ┌──────────────────────────┐
                              │ Flood simulation and     │
                              │ forecasting              │
                              └──────────────────────────┘

                              ┌──────────────────┐
                              │   Model output   │
                              └──────────────────┘
```

997

998   Figure 2 Modelling flow chart of the QMG (Qingmuguan) model.

999

1000   Figure 3 Spatial structure of karst hydrological response units (KHRUs) (Li et al., 2021).

1001

1002   Figure 4 Algorithm flow chart of the improved chaotic particle swarm optimization (ICPSO).

1003

1004   Figure 5 Iteration process of parametric optimization.

1005

1006   Figure 6 Flow simulation results of the QMG model based on parameter optimization.

1007
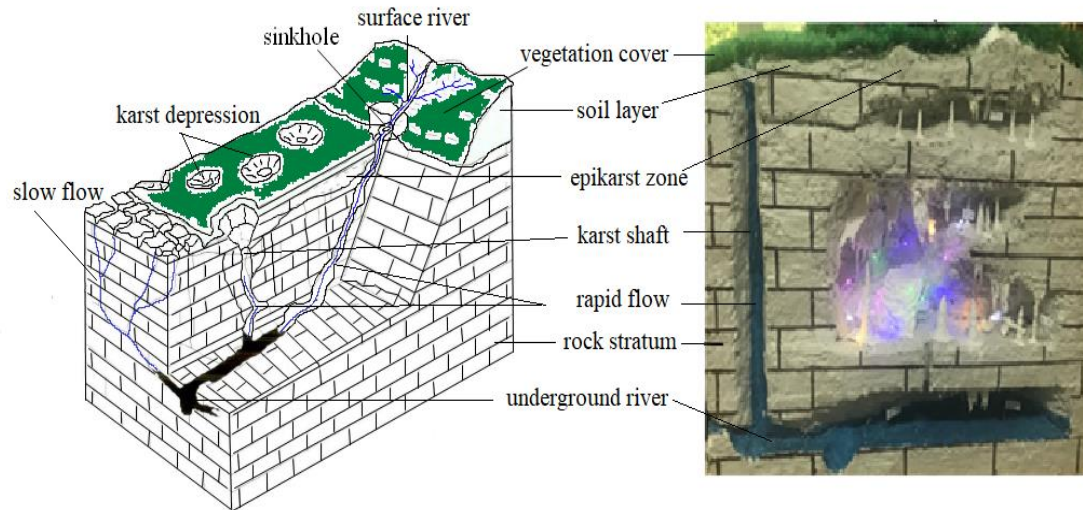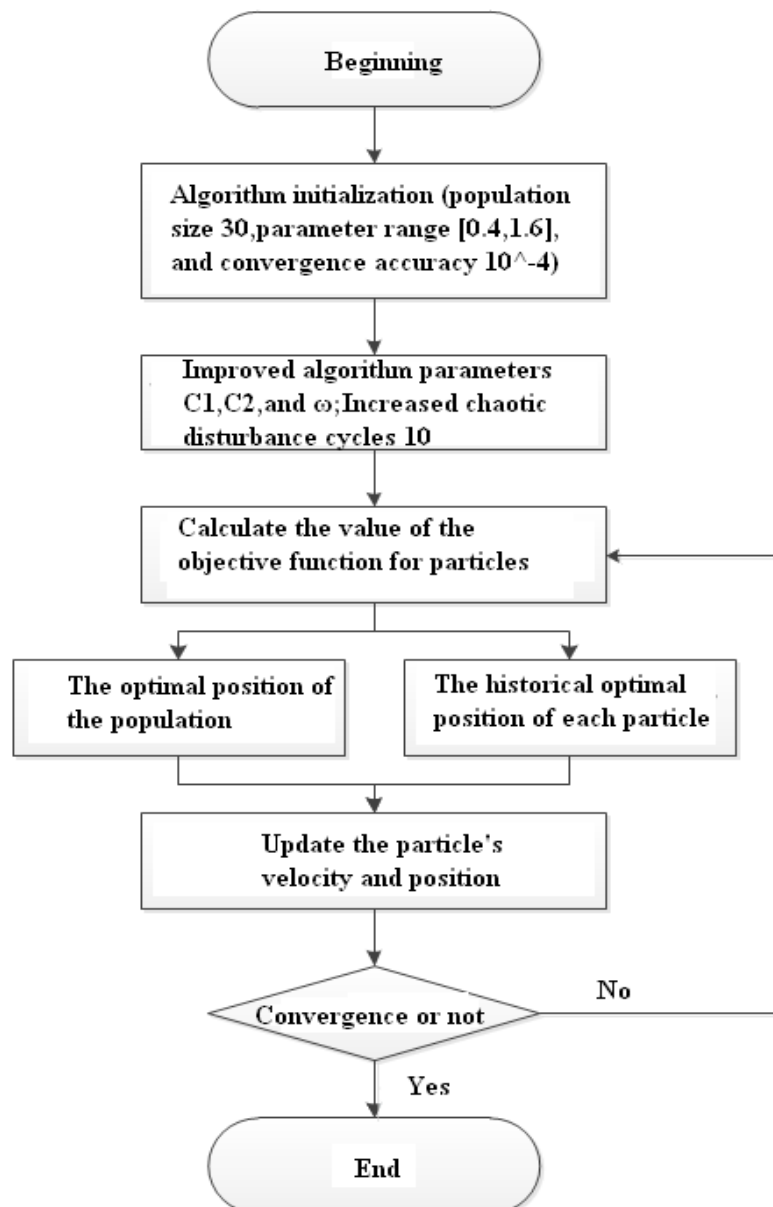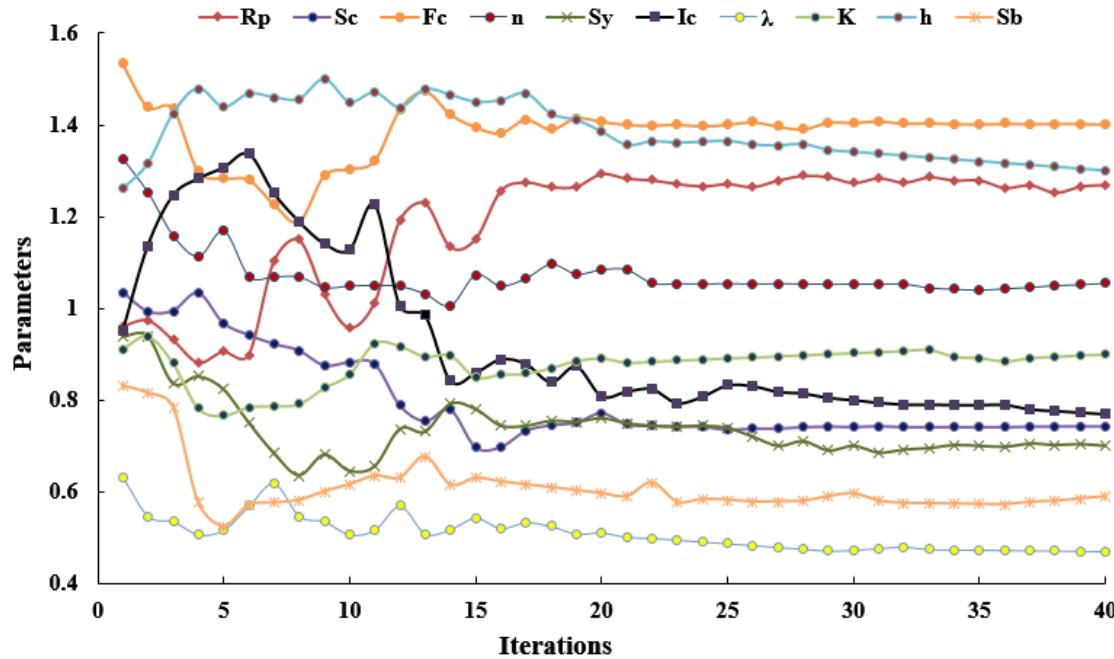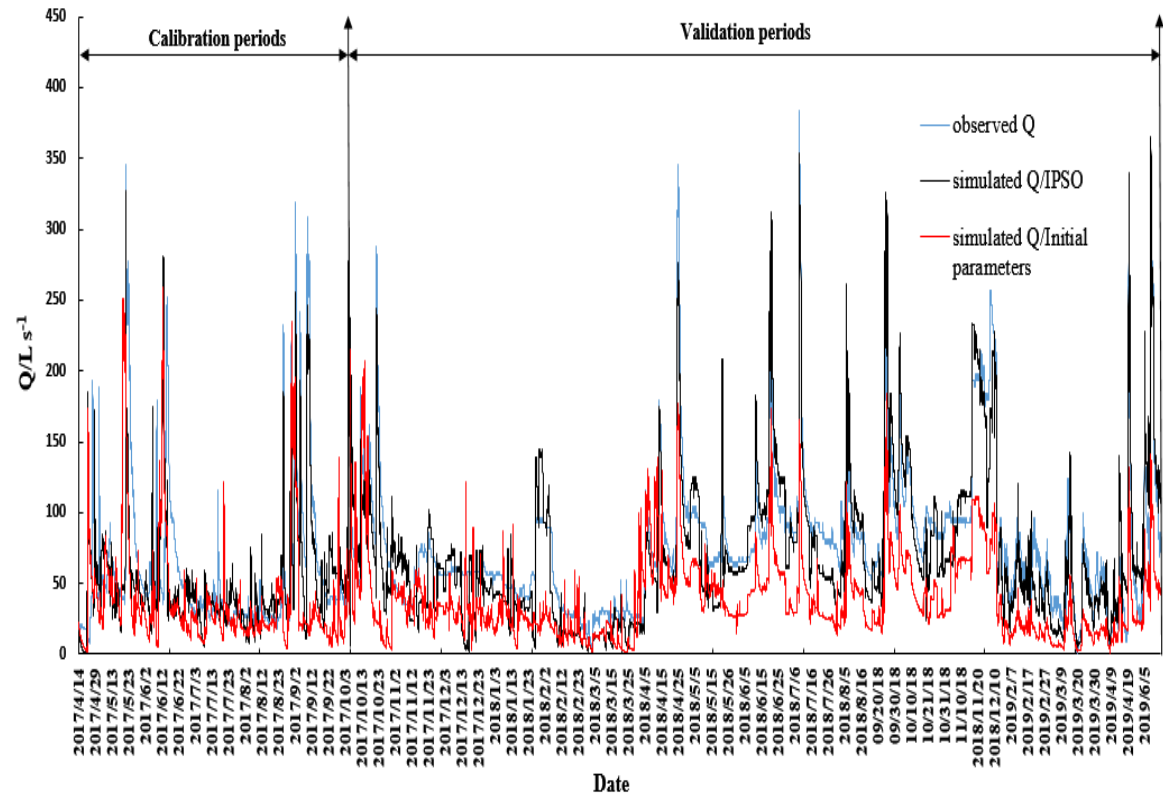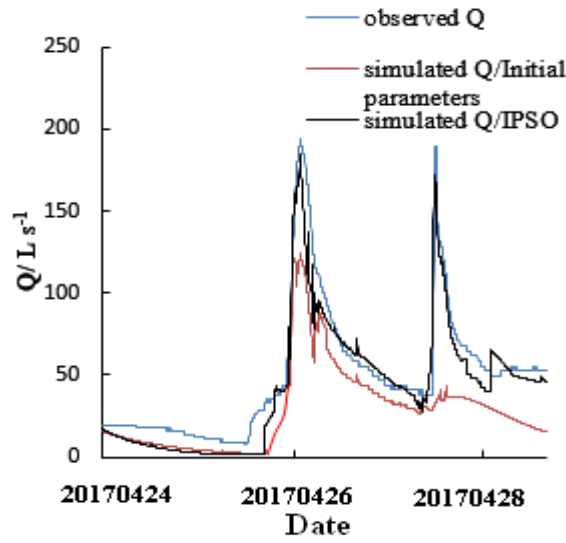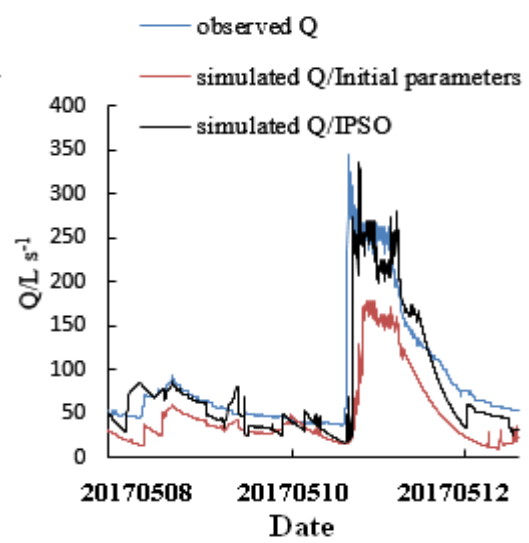
1008   a. flood 201704240800   b. flood 201705081600

1009
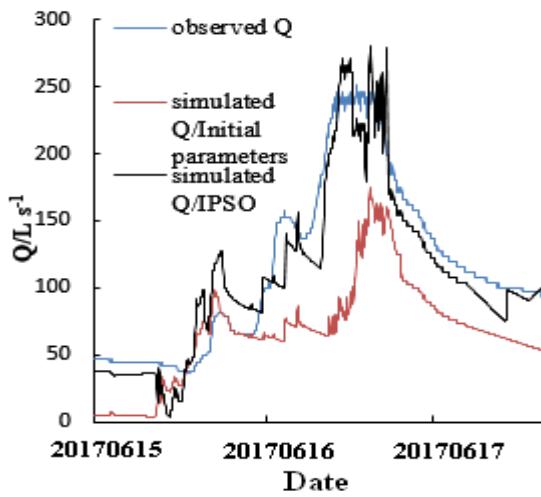
1010   c. flood 201706151800   d. flood 201707101530
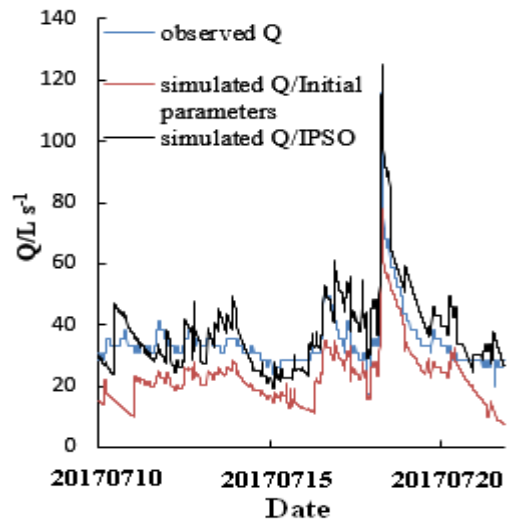
1011
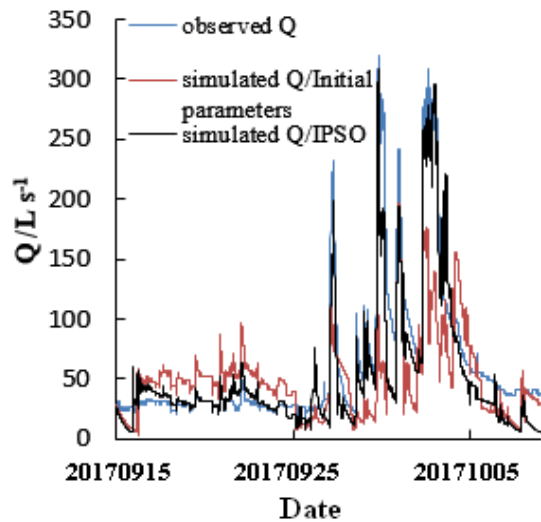
1012   e. flood 201709151200   f. flood 201710081500
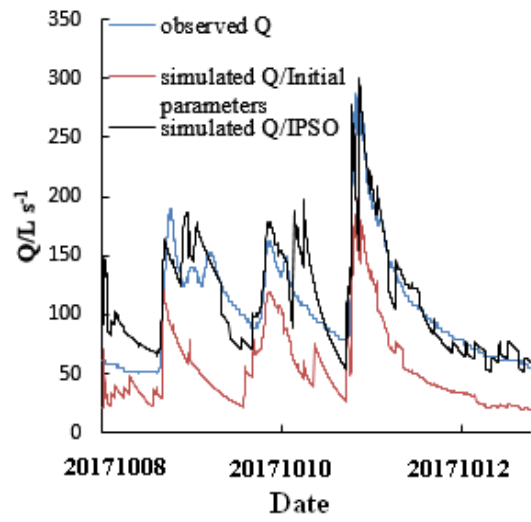
1013
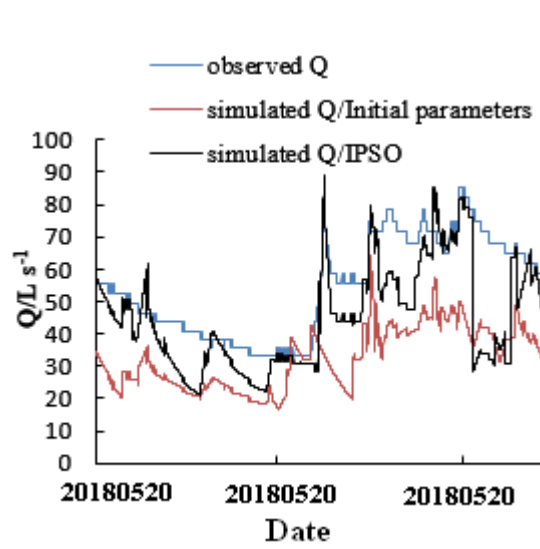
1014   g. flood 201805201600   h. flood 201806081500
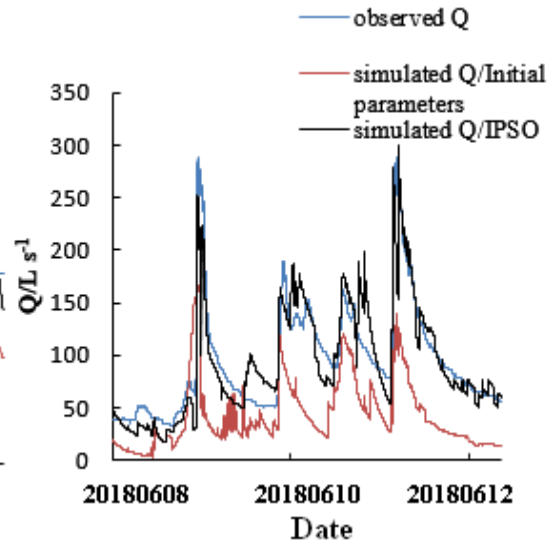
1015
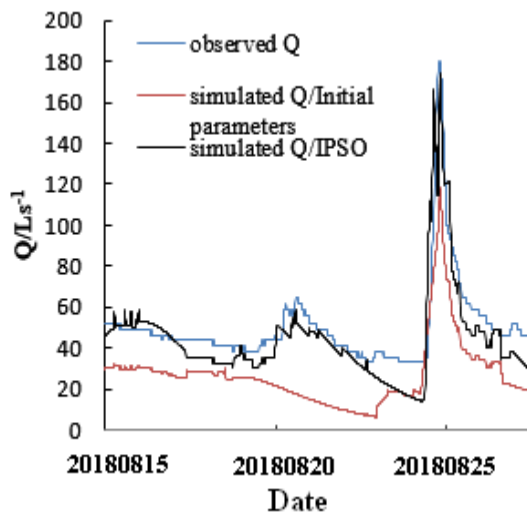
1016   i. flood 201808151200   j. flood 201905251600

1017   Figure 7 Flood simulation effects based on initial and optimized parameters.